



Robust dating of Pb–Zn skarn systems by LA–ICP–MS garnet U–Pb geochronology

Jiadao Li^a, Jing Xu^{b,*}, Shitou Wu^{c,*}, Nigel J. Cook^d, Cristiana L. Ciobanu^d, Sarah Gilbert^e, Liyuan Wang^b

^a School of Tourism and Culture Industry, Chengdu University, Chengdu 610106, China

^b Zijin School of Geology and Mining, Fuzhou University, Fuzhou 350108, China

^c Institute of Geology and Geophysics, Chinese Academy of Sciences, Beijing 100029, China

^d School of Chemical Engineering, The University of Adelaide, Adelaide SA-5005, Australia

^e Adelaide Microscopy, The University of Adelaide, Adelaide SA-5005, Australia

ARTICLE INFO

Keywords:

LA–ICP–MS U–Pb geochronology

Garnet

Pb–Zn skarn

Nyainqentanglha metallogenic belt

Tibet

ABSTRACT

Lawu and Yaguila are two Pb–Zn skarn deposits in the eastern Nyainqentanglha metallogenic belt, central Lhasa subterranean, Tibet. The genesis of Pb–Zn deposits in this belt and the crustal processes leading to their formation remain ill-constrained, mostly because of the lack of precise mineralization ages. We integrate textural information, geochemistry, and *in-situ* garnet U–Pb geochronology to constrain the timing and genesis of Pb–Zn mineralization. Garnets from the two deposits display oscillatory compositional zoning (And₁₄Gr₈₆ to And₁₀₀) and contain variable U contents (0.07–5.3 ppm). Aluminum-rich garnet displays a chondrite-normalized rare earth element (REE) fractionation pattern in which LREEs are depleted relative to flat HREE segments. In contrast, Fe-rich garnet shows LREE-enriched, relatively HREE-poor patterns with positive Eu-anomalies. Uranium concentration is correlated with total REE and Fe components in garnets, implying that U incorporation is largely controlled by coupled substitution mechanisms. The same garnets also contain measurable contents of other metals (up to hundreds of ppm), such as Sn, W, and In. The distribution and fractionation of major and trace elements in zoned garnets record periodic fluid pulses with different compositions during hydraulic fracturing. The new garnet U–Pb data show that the Yaguila deposit formed between 68.5 ± 3.4 and 65.0 ± 4.7 Ma, and the Lawu deposit formed at 54.6 ± 2.9 Ma. Within the geochronological framework of igneous rocks and Pb–Zn mineralization in the Nyainqentanglha metallogenic belt, the new garnet ages suggest a magmatic-hydrothermal origin for related mineralization, with the causative magma likely derived from partial melting of ancient continental material due to rollback and subsequent breakoff of the Neo-Tethys oceanic slab during India–Asia continental collision. This study highlights the opportunities offered by garnet U–Pb dating for elucidating the formation age and ore genesis of base metal skarn systems.

1. Introduction

Magmatic-hydrothermal Pb–Zn deposits contribute a significant proportion of global lead and zinc supply. As the most economically important type of magmatic-hydrothermal Pb–Zn deposits, precise geochronology of Pb–Zn skarn deposits is essential for developing comprehensive genetic models, establishing the correlation between ore formation and geodynamic processes, and providing guidance for mineral exploration. Various attempts have been made to constrain the timing of Pb–Zn mineralization, including Rb–Sr dating of sphalerite

(Nakai et al., 1990; Ostendorf et al., 2017), Re–Os dating of sulfides (Liu et al., 2015; Deng et al., 2016), $^{40}\text{Ar}/^{39}\text{Ar}$ dating of K-bearing minerals (Liu et al., 2012; Zheng et al., 2015a), and U–Pb dating of U-bearing accessory minerals (Cao et al., 2021; Milenkovic et al., 2022). However, in many Pb–Zn deposits, K-bearing minerals, U-bearing accessories and even molybdenite are either scarce or absent altogether, and moreover, their temporal association with ore deposition is not always unequivocal. In addition, studies have shown that the Rb–Sr and Re–Os isotope systems in sulfides relate to secondary inclusions and/or particles within fractures (Liu and Shen, 1998; Hnatyshin et al., 2020). As a result,

* Corresponding authors.

E-mail addresses: xujing3800@126.com (J. Xu), shitou.wu@mail.iggcas.ac.cn (S. Wu).

<https://doi.org/10.1016/j.oregeorev.2023.105565>

Received 31 March 2023; Received in revised form 8 June 2023; Accepted 3 July 2023

Available online 7 July 2023

0169-1368/© 2023 The Author(s). Published by Elsevier B.V. This is an open access article under the CC BY-NC-ND license (<http://creativecommons.org/licenses/by-nc-nd/4.0/>).

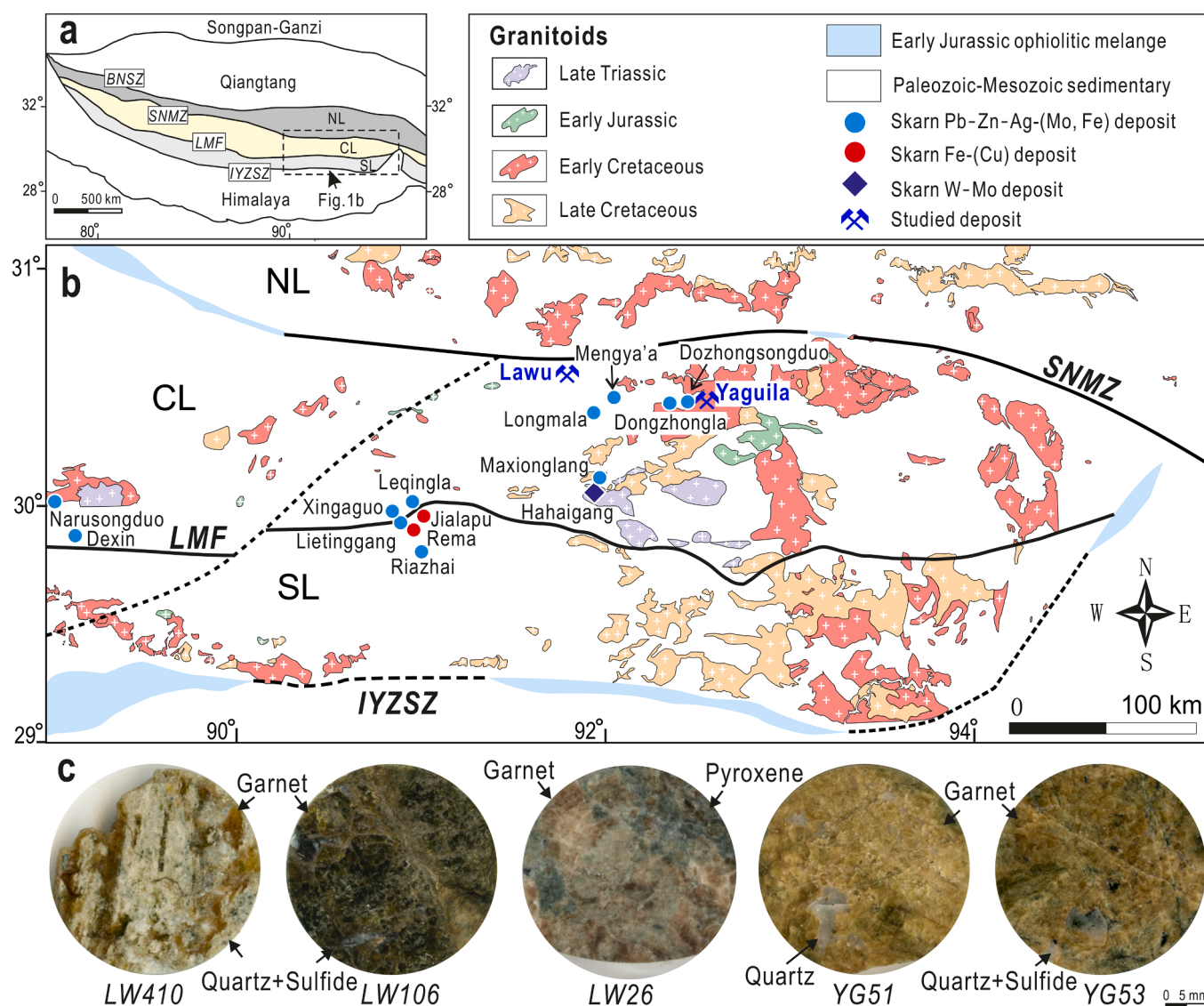
reliable dating of Pb–Zn systems is commonly hampered by a mineralogy unsuitable for isotopic analysis.

Garnet is common in magmatic, metamorphic, and metasomatic rocks. The garnet structure allows for the accommodation of trace uranium and has a high closure temperature for the U–Pb isotope system (0.5 cm-diameter garnet grain > 850 °C; Mezger et al., 1989). Moreover, contemporary analytical systems enable determination of robust garnet U–Pb ages irrespective of the U concentration (Wafforn et al., 2018). These observations reveal the potential of garnet, even when it contains very little U, to provide robust geochronological constraints on skarn genesis. Despite the many studies that have successfully used garnet U–Pb dating (Deng et al., 2017; Seman et al., 2017; Gevedon et al., 2018; Wafforn et al., 2018; Yang et al., 2018; Burisch et al., 2019; Fan et al., 2021; Reinhardt et al., 2022), methodologies are still developing, and more studies are needed to address the utility of garnet U–Pb geochronology to date Pb–Zn mineralization (Li et al., 2018, 2019; Hong et al., 2021; Jiang et al., 2021; Sun et al., 2022; Wen et al., 2022).

The Nyainqentanglha metallogenic belt is located in the central Lhasa subterrane, Tibet, and represents an economically important

Pb–Zn ore province. Several Pb–Zn deposits in this region have unique features whereby either the causative pluton is not exposed, or there is evidence for complex multistage and multi-type ore-forming processes. These scenarios are typified by the Lawu and Yaguila deposits, respectively. The timing of Pb–Zn mineralization in the belt however, remains insufficiently understood, hindering establishment of robust genetic and exploration models. Specifically, there has long been debate over whether these Pb–Zn deposits were formed via submarine exhalative processes (superimposed by magmatic-hydrothermal alteration; Cui, 2012), or alternatively, are the products of magmatic-hydrothermal processes (Zheng et al., 2015c; Xu et al., 2019). Precise and reliable age constraints are also critical for clarifying relationships between multiple episodes of magmatic activity and different styles of mineralization (porphyry Cu ± Au ± Mo mineralization and distal Zn–Pb skarn) within Pb–Zn polymetallic deposits in the belt.

This contribution reports *in-situ* laser-ablation inductively coupled plasma-mass spectrometry (LA–ICP–MS) U–Pb isotope and trace element data for garnet from the Lawu and Yaguila Pb–Zn deposits. The new geochronological results, combined with geochemical data and



published geochronological data, are used to unravel the timing and origin of Pb–Zn mineralization in the region. The applicability of garnet U–Pb geochronology as an effective tool for dating Pb–Zn skarn systems is discussed.

2. Geological background

The Lhasa terrane is a near E–W-trending tectono-magmatic belt with a length of about 2,500 km and a width range of about 150–300 km. The terrane is bounded by the Bangong–Nujiang suture zone (BNSZ) in the north, and the Indus–Yarlung Zangbo suture zone (IYZSZ) in the south (Fig. 1a; Zhu et al., 2011). The terrane can be further divided into the northern Lhasa, central Lhasa (Nyainqêntanglha polymetallic belt), and southern Lhasa subterrane, separated by the Shiquan River–Nam Tso Mélange Zone (SNMZ), and Luobadui–Milashan Fault (LMF)

(Fig. 1b; Zhu et al., 2011). Sedimentary strata in the central Lhasa subterrane are composed of Precambrian metamorphic basement (Nyainqêntanglha Group), Carboniferous–Permian metasedimentary sequences and Upper Jurassic–Lower Cretaceous volcano-sedimentary sequences (Zhu et al., 2011). The central Lhasa subterrane has experienced a complex tectonic-magmatic evolution from Jurassic–Cretaceous Neo-Tethys oceanic subduction, through Cenozoic India – Asia main-collision (65–41 Ma), late-collision transform structural stage (40–26 Ma), and post-collision crustal extension (25–0 Ma) (Yin and Harrison, 2000; Hou et al., 2004; Zheng et al., 2015b). Intensive magmatism occurred from the Late Triassic to the Paleogene (~210–40 Ma), peaking at 110–70 Ma and 55–45 Ma (Xu et al., 2019). Voluminous Mesozoic granitoids with abundant dioritic enclaves (Zhu et al., 2011), Paleocene–Eocene granitoids (Ji et al., 2009), and volcanic rocks of the Linzizong Volcanic Succession (Mo et al., 2008) intruded into sedimentary strata

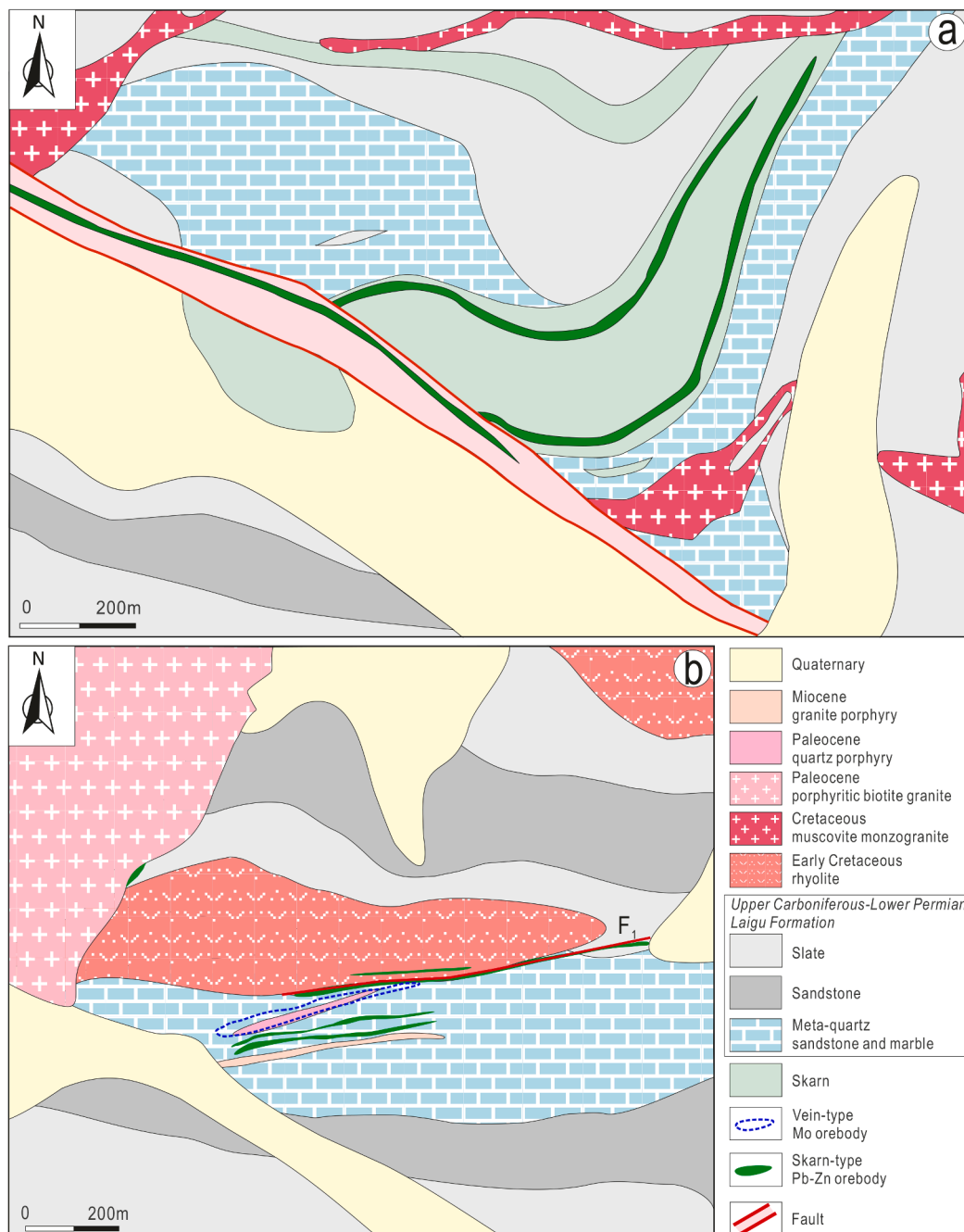


Fig. 2. Geological maps of the (a) Lawu skarn deposit (modified after Du et al., 2004), and (b) Yaguila skarn deposit (modified after Xu et al., 2019).

as large batholiths and stocks. A suite of skarn-type Pb–Zn deposits, such as the Yaguila-Dongzhongla Pb–Zn–Ag ore district, Longmala-Mengya'a Pb–Zn–(Ag) ore district, Xingaguo-Leqingla Pb–Zn ore district, Narusongduo-Sinongduo Pb–Zn–Ag ore district, and Chagele-Longgen Pb–Zn–(Ag) ore district, have been discovered associated with these calc-alkaline intrusions. This makes the Nyainqentanglha polymetallic belt a significant Pb–Zn metallogenic province with considerable additional exploration potential (Zheng et al., 2015c; Zhao et al., 2016; Gao et al., 2021; Jiang et al., 2021).

The Lawu and Yaguila deposits are both located in the eastern section of the Nyainqentanglha metallogenic belt (Fig. 1b). The Lawu skarn

deposit contains a proven reserve of about 26 Mt @ 0.4% Cu, 0.9% Pb, 1.6% Zn, and 35.0 g/t Ag. Outcrop in the Lawu mining area is dominated by quartz sandstone, slate, and marble of the Upper Carboniferous–Lower Permian Laigu Formation. A Cretaceous muscovite monzogranite (109 ± 1.3 Ma, Du et al., 2004) is the only igneous rock exposed. However, skarn-type Pb–Zn mineralization predominantly occurs as EW-trending lamellar or lenticular bodies within slate, quartz sandstone and marble, and to some extent, also within the NW-trending fault (Fig. 2a; Cui, 2012). Neither clear contact relationships between Pb–Zn skarn and Cretaceous muscovite monzogranite, nor endoskarn are observed, indicating that mineralization is distal to the causative

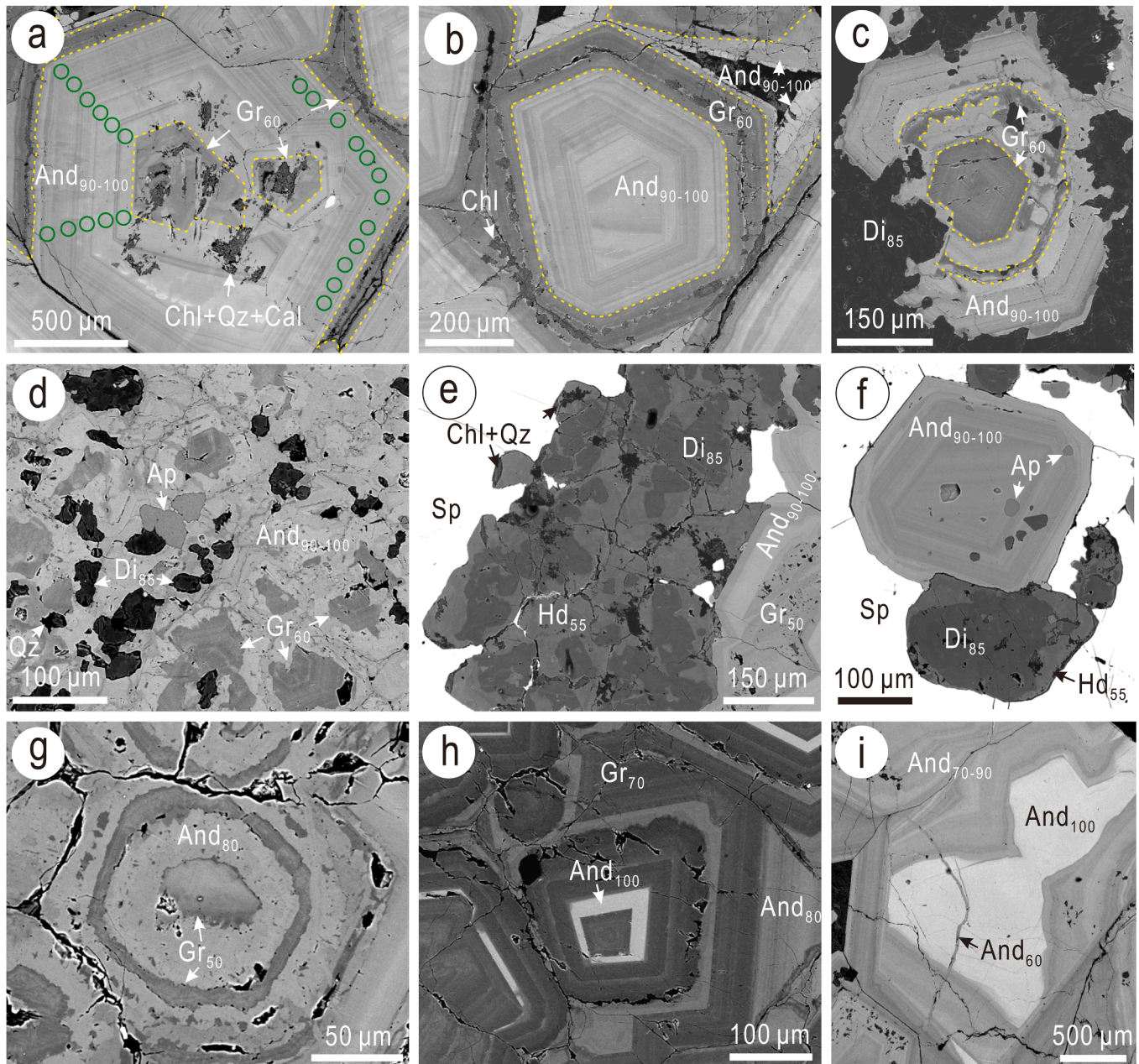


Fig. 3. BSE images showing skarn mineral assemblages at Lawu. (a) Zoned garnet, characterized by a grossular-dominant core (Gr_{60}), oscillatory-zoned andradite mantle (And_{90-100}) and a grossular-dominated rim (Gr_{60}). Abundant pores and microfractures are partly filled with chlorite, quartz, and calcite. (b) Hexagonal andradite (And_{90-100}) surrounded by a grossular-dominant rim (Gr_{60}) that is overprinted by chlorite. (c–d) Zoned garnet consisting of a relict grossular-dominant core (Gr_{60}) and andradite-rich rim (And_{90-100}), marginal andradite coexists with diopside (Di_{85}). (e–f) Coexisting garnet and pyroxene are enclosed by sphalerite; garnet contains a grossular-dominant core (Gr_{50}), an andradite-dominant rim (And_{90-100}), and inclusions of apatite. Pyroxene is composed of diopside-dominated core (Di_{85}) and hedenbergite-dominated rim (Hd_{55}). (g–h) Oscillatory-zoned garnet showing alternating zones that are grossular- and andradite-dominant zones. (i) Zoned garnet showing a pure andradite domain, which is surrounded or cut by a zone of andradite (And_{70-90}) or vein (And_{60}). Green circles represent the location of the Laser ablation pits. Abbreviations: Ap = apatite; Cal = calcite; Chl = chlorite; Qz = quartz; Sp = sphalerite.

intrusion. Skarn-hosted ore is dominant and comprises assemblages of garnet and pyroxene, accompanied by retrograde skarn minerals (e.g., actinolite, clinozoisite, chlorite, quartz, and calcite) and sulfides (e.g., sphalerite, galena, chalcopyrite, pyrrhotite and pyrite) (Fig. 1c and 3).

The Yaguila skarn deposit has reserves of 52 Mt at average grades of 4% Pb, 2% Zn, and 64.3 g/t Ag (Zheng et al., 2015c). The major sedimentary stratum at Yaguila is the Laigu Formation, a sequence of bathyal-abyssal clastic rocks with carbonate rocks. Four types of igneous rocks are recognized: rhyolite (129–127 Ma; Gao et al., 2017), quartz porphyry (~65 Ma, Xu et al., 2019), porphyritic biotite granite (61 Ma, Zhao et al., 2016) and granodiorite porphyry (~17 Ma; Xu et al., 2019). Skarn-type Pb–Zn mineralization primarily occurs as layers or veins in marble, limestone and dolomite of the Laigu Formation, and extends into the overlying Early Cretaceous rhyolitic volcanic rocks (Fig. 2b; Zhao et al., 2016; Xu et al., 2019). Minor porphyry-type Mo mineralization is controlled by faults in the Laigu Formation, and generally occurs as veins or lenses in the Paleocene quartz porphyry and silicified quartz sandstone in its hanging wall (Zhao et al., 2016). Skarn alteration is manifested as prograde garnet, wollastonite, and pyroxene (Fig. 1c and 4), overprinted by retrograde actinolite, clinozoisite, calcite, quartz, and chlorite (Fig. 4e–f). The ore minerals are mainly composed of sphalerite, galena, pyrrhotite, and pyrite with minor chalcopyrite and molybdenite (Fig. 4d), marcasite, and chalcopyrite. Actinolite skarn-hosted ore is the dominant Pb–Zn ore resource, while garnet skarn bears minor disseminations of sphalerite, galena or molybdenite. Although previous studies suggest that these Pb–Zn skarns relate to Paleocene quartz porphyry containing minor Mo mineralization (Xu et al., 2019), the causative igneous rock associated with the skarns remains uncertain, compounded by the lack of any obvious skarn zonation or endoskarn in the orefield.

3. Analytical methods

3.1. Backscattered electron imaging and energy-dispersive spectrometry

One-inch diameter polished blocks were investigated at Adelaide Microscopy, The University of Adelaide, using a FEI Quanta 450 scanning electron microscope (SEM) equipped with a back-scattered electron (BSE) detector and energy-dispersive X-ray spectrometer (EDS). Both BSE and EDS analysis were performed at an accelerating voltage of 20 kV and beam current of 10 nA to characterize textural features, mineralogical relationships, and obtain semi-quantitative compositional data for the dominant skarn minerals within representative samples. Count times for EDS analysis were 60 s per spot.

4. Laser ablation inductively coupled - plasma-mass spectrometry

4.1. Trace element analysis

Trace element data were obtained by LA–ICP–MS using a RESOLUTION-LR 193 nm Excimer laser microprobe coupled to an Agilent 7900x Quadrupole ICP–MS at Adelaide Microscopy, The University of Adelaide. A 51 μm spot size was adopted with 3.5 J/cm² energy density and 5 Hz repetition rate. Each spot analysis consisted of ~30 s of background acquisition and ~50 s of sample data acquisition. Standard reference materials were NIST SRM 610 and GSD-1G, preferred values from the GeoReM database (Pearce et al., 1997; Jochum et al., 2016). Standards were run after each batch of 20 ~ 26 unknowns; detection limits were calculated for each element in each spot analysis. Internal calibration was achieved using concentration values of ⁴³Ca (garnet and pyroxene), obtained from EDS data. The following basic set of isotopes were monitored: ⁷Li, ²³Na, ²⁴Mg, ²⁷Al, ²⁹Si, ³¹P, ³⁹K, ⁴³Ca, ⁴⁵Sc, ⁴⁹Ti, ⁵¹V, ⁵²Cr, ⁵⁵Mn, ⁵⁷Fe, ⁵⁹Co, ⁶⁰Ni, ⁶⁵Cu, ⁶⁶Zn, ⁶⁹Ga, ⁷⁵As, ⁸⁵Rb, ⁸⁸Sr, ⁸⁹Y, ⁹⁰Zr, ⁹³Nb, ⁹⁵Mo, ¹¹⁵In, ¹¹⁸Sn, ¹²¹Sb, ¹³³Cs, ¹³⁷Ba, ¹³⁹La, ¹⁴⁰Ce, ¹⁴¹Pr, ¹⁴⁶Nd, ¹⁴⁷Sm, ¹⁵³Eu, ¹⁵⁷Gd, ¹⁵⁹Tb, ¹⁶³Dy, ¹⁶⁵Ho, ¹⁶⁶Er, ¹⁶⁹Tm, ¹⁷²Yb,

¹⁷⁵Lu, ¹⁷⁸Hf, ¹⁸¹Ta, ¹⁸²W, ²⁰⁶Pb, ²⁰⁷Pb, ²⁰⁸Pb, ²³²Th and ²³⁸U for skarn minerals. Data reduction was performed using Iolite, an open-source software package for processing ICP–MS data (Paton et al., 2011). LA–ICP–MS trace element mapping was conducted using the same LA–ICP–MS system. Element maps were created by ablating sets of parallel line rasters in a grid across the sample. The effect of redeposition during mapping was minimized by pre-ablating each line prior to the main data collection run. A beam size of 16 μm and scan speeds of 16 $\mu\text{m/s}$ were employed for all samples. These parameters resulted in the desired sensitivity of the elements of interest, and adequate spatial resolution. A laser repetition of 10 Hz was selected with an energy density of 3.5 J/cm² at the target. A 30-s background acquisition was acquired at the start of every raster, and to allow for cell wash-out, gas stabilization, and computer processing, a delay of 15 s was used after each line. Reference materials GSD-1G and NIST-610 were run at the start and end of each mapping run. Images were compiled and processed using the program Iolite (Paton et al., 2011). To correct for instrument drift during a typical 4–8 h-long mapping run, standards were analyzed immediately before and after the run. If present, a correction was applied using a linear fit between the two sets of standards. Following this, the average background intensity of every element was subtracted from its corresponding raster, the resultant time resolved intensities compiled into a 2-D image displaying combined background/drift corrected intensity for each element.

4.2. U–Pb isotope analysis

In situ U–Pb isotope experiments were undertaken using an Element XR SF-ICP–MS instrument (Thermo Fisher Scientific, America) coupled with an excimer 193 nm laser ablation system (Geolas HD, Coherent, Germany), located at Institute of Geology and Geophysics, Chinese Academy of Sciences. The Element XR is equipped with the so-called “jet-interface”, comprising of a jet sample cone, an X-version skimmer cone and a high-capacity vacuum pump (OnTool Booster 150, Asslar, Germany). This leads to a signal enhancement in laser sampling mode by a factor of 3–5, resulting in an improved detection capability (Wu et al., 2020). Helium was used as carrier gases through the ablation cell and mixed with argon downstream of the ablation cell. A spot size of 60 μm , repetition rate of 8 Hz, and a fluence of ~10 J/cm² were used for garnet measurements. Each analytical session used the same spot size for standard and unknowns. Each spot analysis consisted of an approximately 25 s background and 60 s sample data acquisition. A well-characterized matrix-matched external reference material of known age is fundamental to LA–ICP–MS U–Pb analysis. Dedicated external reference materials for andradite U–Pb geochronology: Willsboro andradite (1022 ± 16 Ma; Seman et al., 2017); and Mali Red garnet (202 ± 2 Ma; Seman et al., 2017), were used in this study to correct for U–Pb fractionation and instrumental mass discrimination. Reference glasses NIST SRM 614 and ARM-3 (Wu et al., 2019; Wu et al., 2021) were used as external standards to calibrate trace element concentrations in garnets; ⁴³Ca served as the internal standard. Garnet U–Pb ages were determined using linear regressions on Tera–Wasserburg diagram (Tera and Wasserburg, 1972). The lower intercept age on the Tera–Wasserburg diagram is selected to represent the crystallization age of analyzed garnet. All isotopic data for garnet grains were processed using GLITTER software (Van Achterbergh, 2001) and ISOPLOT/EX 3.23 (Ludwig, 2003).

5. Results

5.1. Mineral textures and major element compositions

EDS results for garnet and pyroxene from the Lawu and Yaguila deposits are tabulated in Electronic Appendix Tables A1 and A2, respectively, and depicted on Fig. 5. Lawu garnet is up to 5 mm in size, mainly subhedral to euhedral (Fig. 3), and the composition ranges from

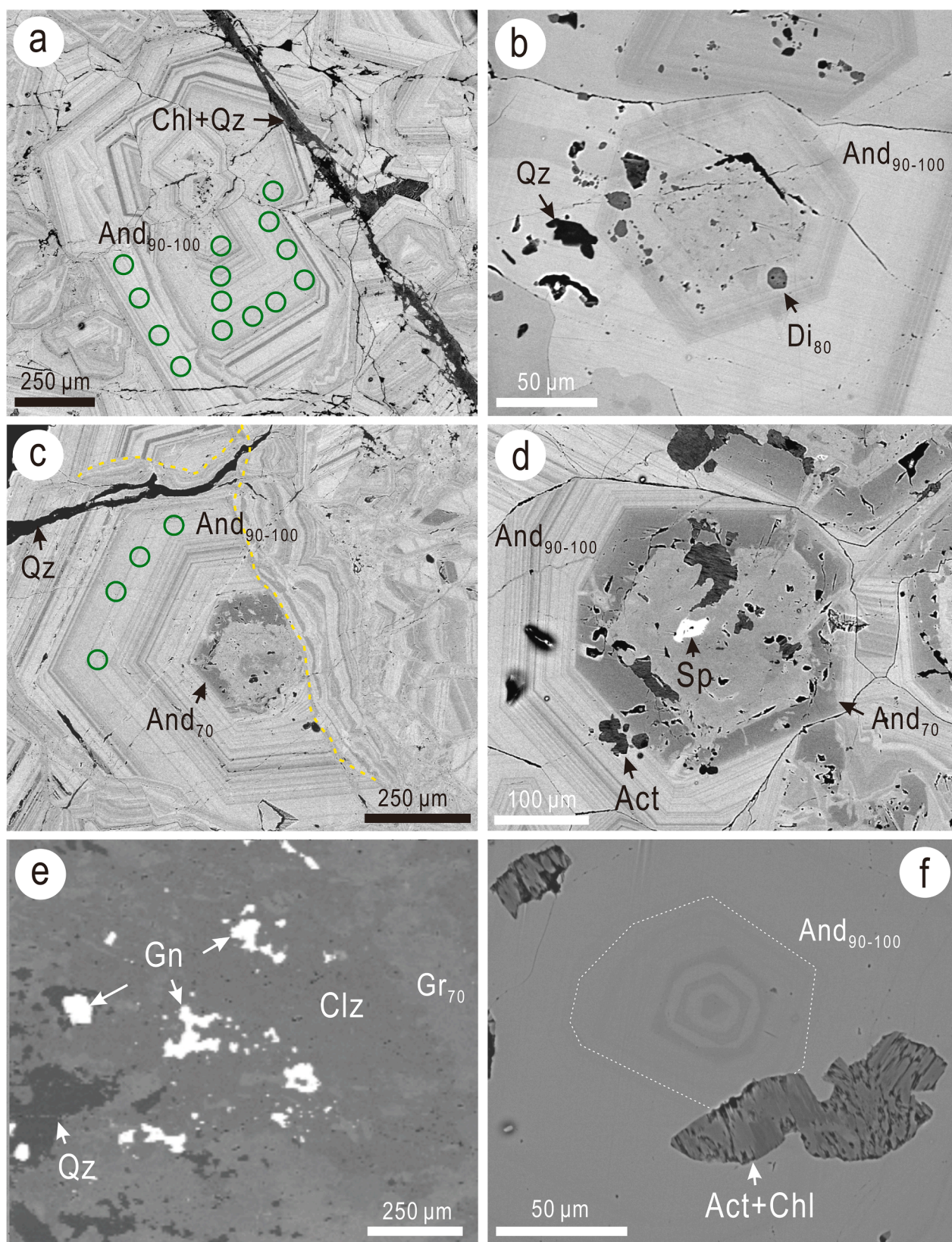


Fig. 4. BSE images showing skarn mineral assemblages at Yaguila. (a) Oscillatory-zoned andradite (And₉₀₋₁₀₀), cut by chlorite and quartz. (b) Diopside (Di₈₀) inclusion in andradite (And₉₀₋₁₀₀), replaced by quartz. (c-d) Zoned garnet showing heterogeneous relict cores (And₇₀) and oscillatory-zoned rims (And₉₀₋₁₀₀), overprinted by actinolite and sphalerite. (e) Galena occurs interstitial to clinozoisite. (f) Zoned andradite replaced by actinolite and chlorite. Green circles in (a) and (c) represent the location of the Laser ablation pits. Abbreviations: Act = actinolite; Chl = chlorite; Clz = clinozoisite; Qz = quartz; Sp = sphalerite.

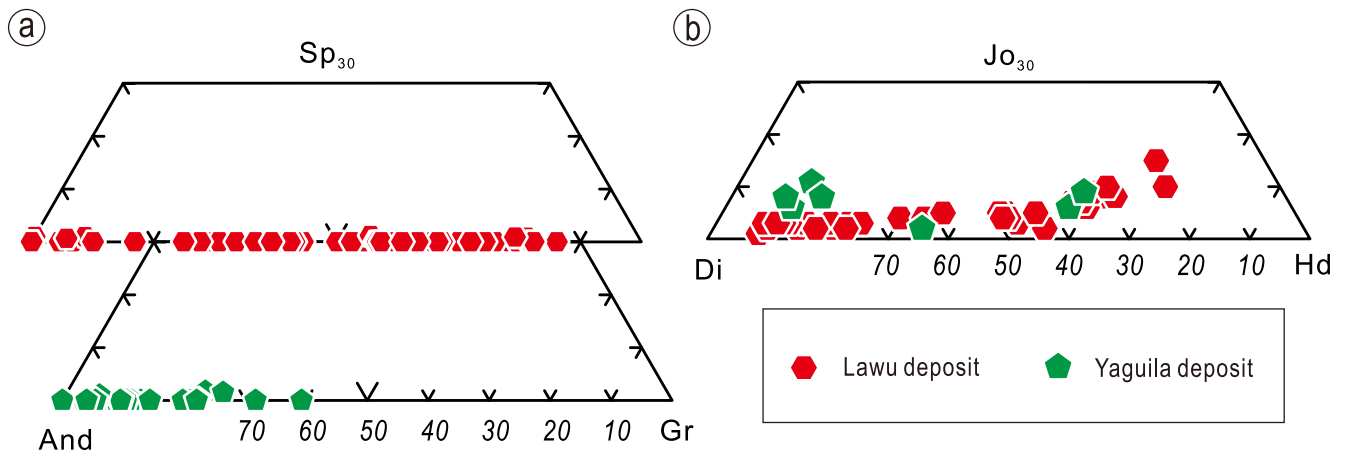


Fig. 5. Ternary diagrams illustrating compositions of garnets (a) and pyroxenes (b) from the Lawu and Yaguila deposits. Abbreviations: And = andradite; Di = diopside; Gr = grossular; Hd = hedenbergite; Jo = johannsenite; Sp = spessartine.

endmember andradite (And₁₀₀) to grossular (And₁₄Gr₈₆) (Fig. 5a). From the interior to the margin of individual garnet grains, domains with different brightness and distinct boundaries, expressed by sharp variations in Fe/Al ratio, are illustrated in BSE images (Fig. 3a-c, g-i). Inner zones are typically characterized by relict core, dominated by Fe-rich

grossular (Gr₅₀₋₆₀; Fig. 3a, c-e, g). The intermediate and outer zones display concentric, oscillatory zones with compositions that alternate between andradite (And₈₀₋₁₀₀) and Fe-rich grossular (Gr₅₀₋₇₀; Fig. 3a-c, g-h). These textural characteristics indicate the discontinuous precipitation of garnet. Lawu garnets feature abundant pores and extensive

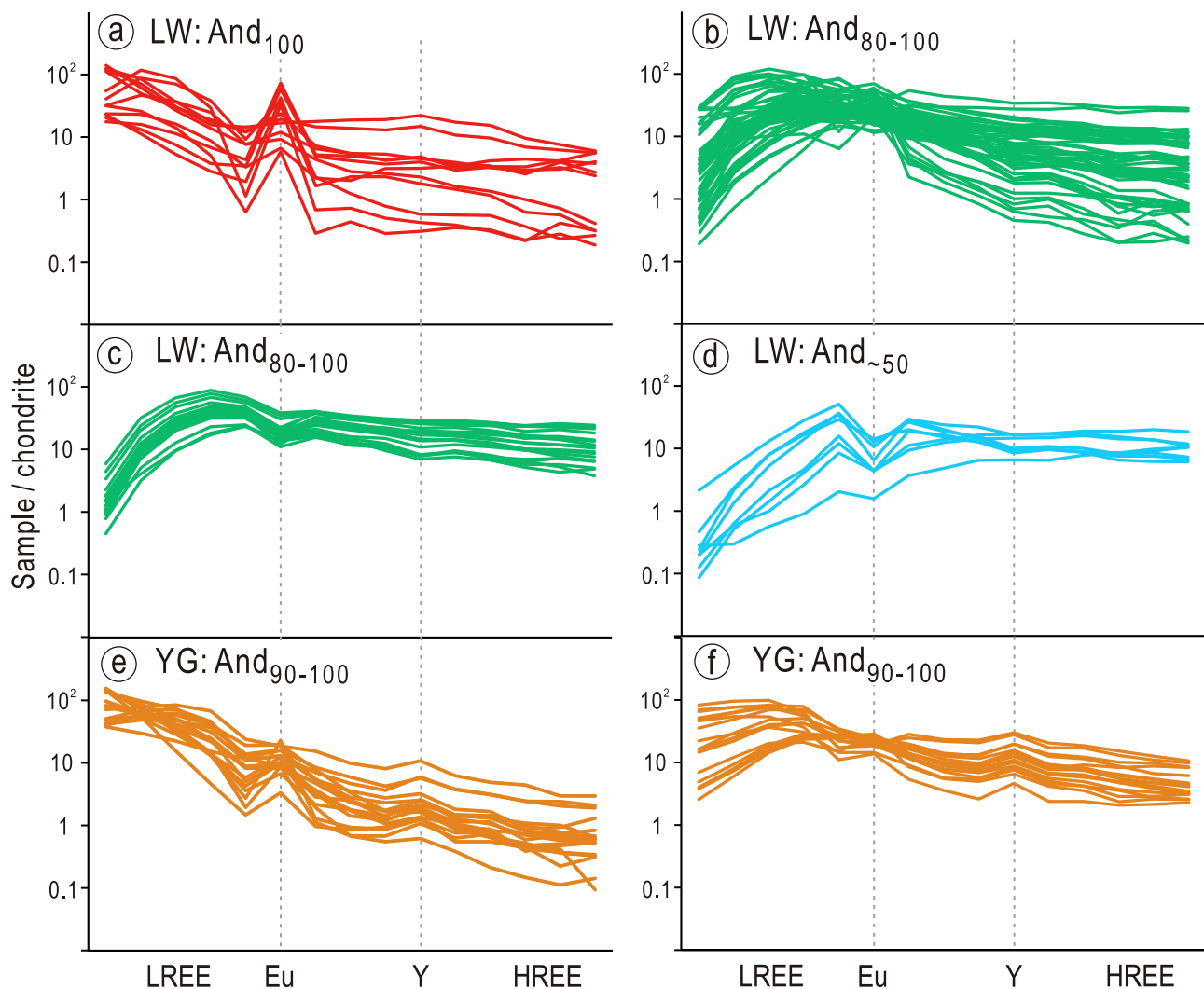


Fig. 6. Chondrite-normalized REY fractionation patterns for garnets from the Lawu (a-d) and Yaguila (e-f) deposits.

microfracturing and therefore are susceptible to late-stage alteration that results in an assemblage of chlorite, quartz, and calcite (Fig. 3a-b). Coexisting pyroxene has an endmember formula of $\text{Di}_{18-93}\text{Hd}_{7-71}\text{Jo}_{0-15}$ (Fig. 5b). Core-rim texture is observed in the Lawu pyroxene (Fig. 3e-f), characterized by a Mg-rich core (Di_{85}) and Fe-rich rim (Hd_{55}). Sphalerite is mostly interstitial to the skarn minerals and also occurs within various matrix assemblages (Fig. 3e-f). Notably, pyroxene composition is closely related to those of coexisting garnet: diopside is texturally associated with andradite (Fig. 3d), whereas hedenbergite is usually found together with grossular. This is indicative of changes in fluid oxidation condition during formation.

Yaguila garnet mainly occurs as relatively coarse (>1 mm) euhedral crystals, and relatively limited compositional variation from andradite (And_{100}) to Al-rich andradite ($\text{And}_{59}\text{Gr}_{41}$) (Fig. 5a). Most garnets have heterogeneous relict cores ($\text{And}_{\sim 70}$) and oscillatory zoned rims (And_{90-100}) (Fig. 4c-d). Coexisting pyroxene is scarce and has the composition $\text{Di}_{33-83}\text{Hd}_{9-58}\text{Jo}_{2-11}$ (Fig. 5b). Diopside-rich pyroxenes (Di_{80}) can occur included in andradite (And_{90-100}) (Fig. 4b). Retrograde alteration assemblages, comprising actinolite, chlorite, and quartz, are formed via replacement of anhydrous garnet and pyroxene (Fig. 4). Sphalerite and galena commonly occur in pores or interstices within skarn minerals (Fig. 4d-e).

5.2. Trace element compositions

Rare earth element (REE) distributions in each sample were normalized to chondrite values of McDonough and Sun (1995). Yttrium is plotted between Dy and Ho, following established practice. Compositional data for garnet from the Lawu and Yaguila deposits and

pyroxene from the Lawu deposit are tabulated in [Electronic Appendix Tables B1 and B2](#) and illustrated in [Figs. 6 and 7](#).

5.3. Garnet

Trace element concentrations in garnet show pronounced variation and are largely dependent on major oxide composition. Chondrite-normalized REY fractionation trends are summarized in [Fig. 6](#).

In the Lawu deposit, endmember andradite (And_{100}) features a LREE-enriched, relatively HREE-poor fractionation pattern, with conspicuous positive Eu-anomalies (Fig. 6a). Comparable patterns are observed in Fe-rich garnet (And_{80-100}), albeit with a marked depletion in La and Ce, as well as small, generally negative but variable Eu-anomalies (Fig. 6b-c). The Al-rich garnet ($\text{And}_{\sim 50}$) mostly displays a fractionation pattern in which LREEs are depleted relative to flattish HREE segments, and no apparent Eu-anomalies are noted (Fig. 6d). Similarly, Fe-rich garnet (And_{90-100}) from the Yaguila deposit shows LREE-enriched, relatively HREE-poor patterns, with weak positive Eu-anomalies (Fig. 6e-f), nevertheless some show slight depletion of La and Ce (Fig. 6f).

Analysis of garnets from Lawu and Yaguila confirm the presence of significant concentrations of other trace elements ([Electronic Appendix Tables B1](#)). These include large ionic lithophilic elements (LILE), high field strength elements (HFSE), and transition metals commonly reported in garnet, such as Sc, Ti, V, and Cr, but also the systematic presence of measurable Sn, W, As, In, and to a lesser extent, also U ([Electronic Appendix Tables B1 and Fig. 7](#)). Yaguila garnet contains up to 73 ppm In, and Lawu garnet contains both In (up to 58 ppm) and Sn (up to 8680 ppm). The high concentrations of both In and Sn in garnet (Fig. 7b) correlate with the metallogenic signature of the Lawu deposit,

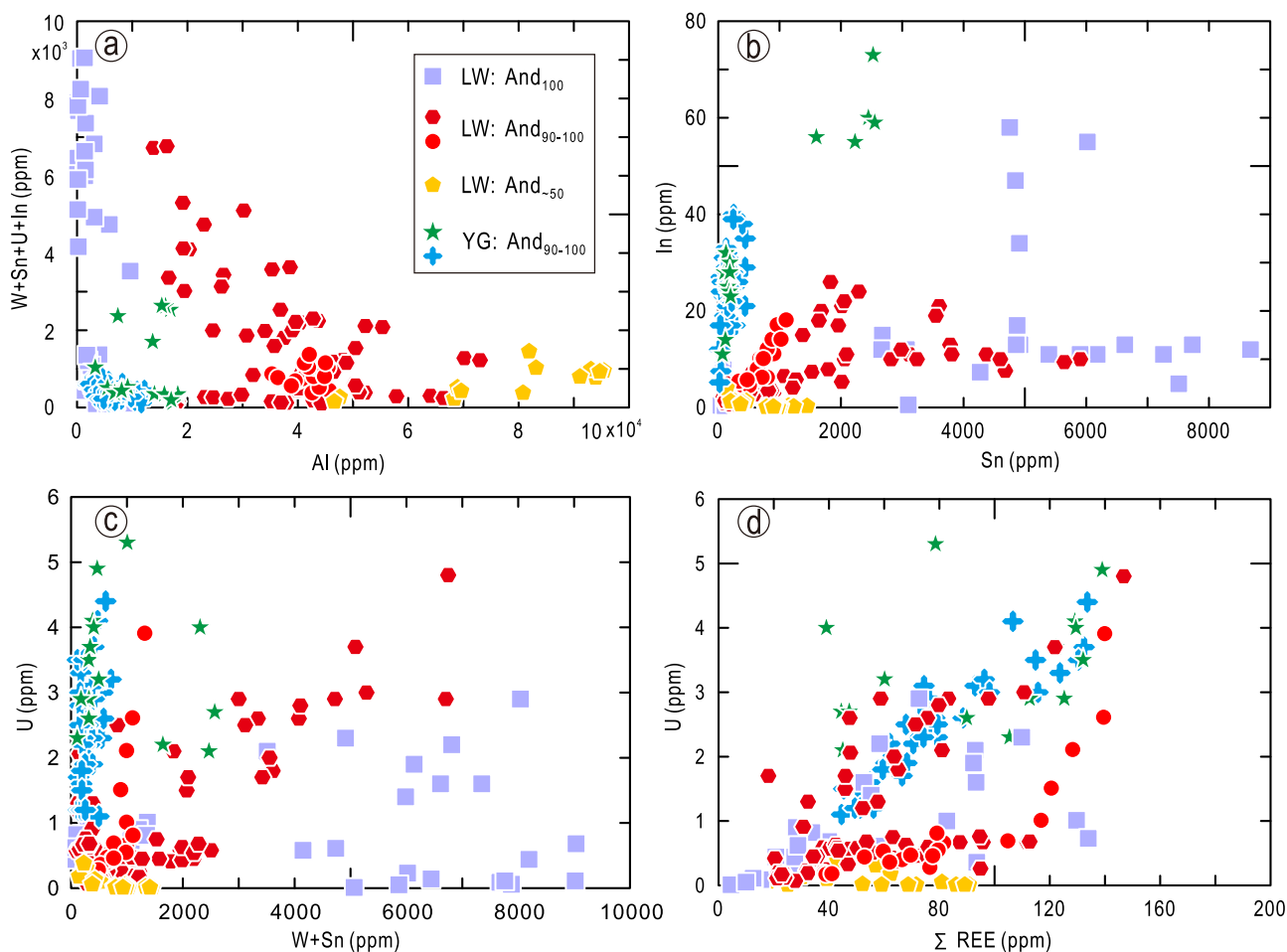


Fig. 7. Scattergrams of Al vs. W + Sn + U + In (a), Sn vs. In (b), Sn vs. U (c), and ΣREE vs. U (d) in garnets at Lawu and Yaguila.

which also features high concentrations of In (~500 ppm) in sphalerite and Sn (200–400 ppm) in chalcopyrite (unpublished data). Garnets contain measurable U (up to ~5 ppm) in both deposits.

Grain-scale trace element distributions in zoned garnet were investigated and visualized by LA-ICP-MS element mapping (data for Lawu and Yaguila in Figs. 8 and 9, respectively). All the garnet textural domains (i.e., core, mantle, and rim) show strong zonation in some trace elements. Commonly, albeit not exclusively, the mantles of Fe-rich Lawu garnet are defined by elevated HFSE (Zr, Ti, U, Sc, REY) and other elements (W, Sn, As) (Fig. 8). Correlations and common zoning trends among Fe, W, Sn, As (and also U although less well correlated), are clearly observed. Titanium and Zr mimic one another and are clearly antithetic to Sc, which behave as REE, particularly La. Marked differences and even inverse correlations exist between individual REE (e.g., La and Sm) and Y. Oscillatory zoning well expressed by elements of various groups is observed in Yaguila garnet (Fig. 9). Concentrations of In in Yaguila garnet exhibit a distinct positive correlation with Sn and Eu, but a strong negative correlation with W and La. Similarly, Ti and Zr display consistent behaviors in Yaguila garnet, but are subtly distinct from other transition metals such as V and Mn. Uranium concentrations vary in rough accordance with REE, confirming the results of spot analysis (Fig. 7d).

5.4. Pyroxene

Pyroxene, especially diopside, from the Lawu deposit is evidently poor in total REY (Di: <2.7 ppm, Hd: mostly <11 ppm, [Electronic Appendix Tables B2](#)). Despite the low concentrations, both diopside and hedenbergite are relatively enriched in LREE and depleted in HREE. Lawu pyroxene, irrespective of major element composition, contains measurable concentrations of Na, K, Sc, Ti, V, Cr, Co, Ni, Zn, Ga, and As ([Electronic Appendix Tables B2](#)).

5.5. Garnet U–Pb ages

U–Pb isotope data from garnets are tabulated in [Table 1](#) and illustrated in [Fig. 10](#). Three garnet samples with high andradite components (And_{80–90}) were collected from the ore-bearing skarns in the Lawu and Yaguila deposits. Bright and homogeneous zones under BSE imaging were targeted for dating in order to avoid potentially ambiguous results derived from multiple growth zones, which are common in both deposits (Figs. 4 and 5). Error ellipses for LA-ICP-MS U–Pb analyses scatter along linear arrays on the Tera-Wasserburg diagrams ([Fig. 10](#)), due to variations in common Pb and U contents. Data spread enables regression of the common Pb mixing line. Lawu garnet sample yields a lower intercept age at 54.6 ± 2.9 Ma ([Fig. 10a](#)), and the Yaguila garnets show overlapping lower intercept ages between 68.5 ± 3.4 Ma and 65.0 ± 4.7 Ma ([Fig. 10b](#)).

6. Discussion

6.1. Linking zonation in garnet to its formation

The distribution and fractionation of major and rare earth elements in zoned garnet provide insights into changes in environment of skarn formation (P, T, pH, oxidation state), fluid chemistry, and even trace fluid-rock interaction and hydrothermal fluid evolution (Sverjensky, 1984; Bau, 1991; Jamtveit et al., 1993; Van Westrenen et al., 2000; Smith et al., 2004; Gaspar et al., 2008; Xu et al., 2016, 2020; Park et al., 2019; Wang and Duan, 2021). The widespread oscillatory zonation observed in garnets from Lawu and Yaguila mirrors that reported by Jamtveit et al. (1993) with respect to an oscillatory intergrowth of andradite with a grossular-rich core (Figs. 4 and 5), implying periodic fluid flow during hydraulic fracturing. Keankeo and Hermann (2002) examined the formation of oscillatory zonation in skarn garnets and made the point that Fe-rich zones crystallize at high fluid flow during the

hydro-fracturing state, with increase in temperature and fO_2 , as well as decrease in pressure, whereas Al-rich zones precipitate at steady state conditions after the fluid pulse. Zones appearing dark on BSE images with increasing grossular component that occur in the Lawu garnet are characterized by peak concentrations of MREE and HREE rather than LREE (Pr and Nd) in andradite-rich zones, while the brightest zones consisting of pure andradite are particularly enriched in La or Ce relative to other REE ([Fig. 6a–d](#)). These fractionation trends resemble those reported by Park et al. (2019) and summarized by Wang and Duan. (2021), indicating intermittent equilibrium crystallization (Van Westernen et al., 2000) and non-equilibrium crystallization via a surface adsorption mechanism (Gaspar et al., 2008), respectively. Collectively, Lawu and Yaguila garnets crystallized from periodic fluid flow with repetitive composition variation during hydraulic fracturing: the bright domains containing greater Fe content formed in disequilibrium during the pressure release state, and the dark domains containing more Al content in equilibrium during the steady state (Figs. 4 and 5). Previous studies have suggested that the characteristics of the Eu-anomaly in garnet are constrained by changes in crystallization and decomposition of minerals that preferentially host Eu, evolving oxidation states, and REE speciation of hydrothermal fluid, especially the presence of complexing agents such as Cl^- (Sverjensky, 1984; Bau, 1991; Wang and Duan, 2021). In Lawu garnet, drastic changes in Eu-anomaly from positive to negative may reveal major shifts in fluid salinity, from high to low, during formation (Smith et al., 2004; Xu et al., 2016).

Other trace elements in oscillatory-zoned skarn garnet can also reveal their relative abundances in skarn-forming fluids and thus provide information with respect to changes in physicochemical condition and fluctuations in fluid composition caused by fluid pulses (Jamtveit et al., 1993; Park et al., 2019). Changes in fluid oxidation state might be concomitant with variable incorporation of multi-valence elements (e.g., Sn, W, and U) into garnet structure. Tin and W prefer to substitute into the octahedral site of garnet in their oxidized states (Dhivya et al., 2013; Xu et al., 2016; Park et al., 2019), whereas U is more likely incorporated into the dodecahedral site in its reduced state, although some substitution into the octahedral site with higher oxidation states (U^{5+} , U^{6+}) may also occur (Smith et al., 2004; Gaspar et al., 2008; Guo et al., 2016). In our study, the behaviors of Sn and W in zoned garnets, especially those from Yaguila, are distinct (Figs. 8 and 9), while moderate correlations between U and W, Sn are observed, especially in Lawu garnets ([Fig. 7c](#), 8 and 9). In this case, instead of changes in fO_2 , other controlling factors might account for the observed compositional variation among these elements in zoned garnets. Bright bands in studied garnets, enriched in Fe, W, and As (Figs. 8 and 9), coincide with zonation patterns reported in garnet by Jamtveit et al. (1993), indicative of externally buffered fluid pulses with different composition, following the model proposed by Yardley et al. (1991).

6.2. Incorporation of U into garnet

High-magnification BSE imaging reveals the absence of visible U-rich mineral inclusions, implying that the U is dominantly hosted within the garnet structure. Incorporation of U, REE³⁺ and Y into the dodecahedral site of garnet is commonly accompanied by coupled substitution to achieve charge balance (Shannon, 1976; Smith et al., 2004). In terms of REY partitioning trends into garnets with different major element compositions (And vs. Gr), the garnets at Lawu and Yaguila follow trends analogous to those reported by Smith et al. (2004) and Gaspar et al. (2008), among others. Such similarity suggests the coupled substitution mechanism: $REE_{VIII}^{3+} + Z_{IV}^{3+} = X_{VIII}^{2+} + Si_{IV}^{4+}$, where Z is typically Si^{4+} (substituted by Al, Fe³⁺, Ti, and P) in tetrahedral coordination, and X is divalent cations (Ca, Mg, Mn, and Fe²⁺) in octahedral coordination. An increase in Fe³⁺ cations within the contiguous tetrahedral position may reduce the incorporation energy required for U and REE occupancy in the dodecahedral position (Rák et al., 2011; Deng et al., 2017; Duan

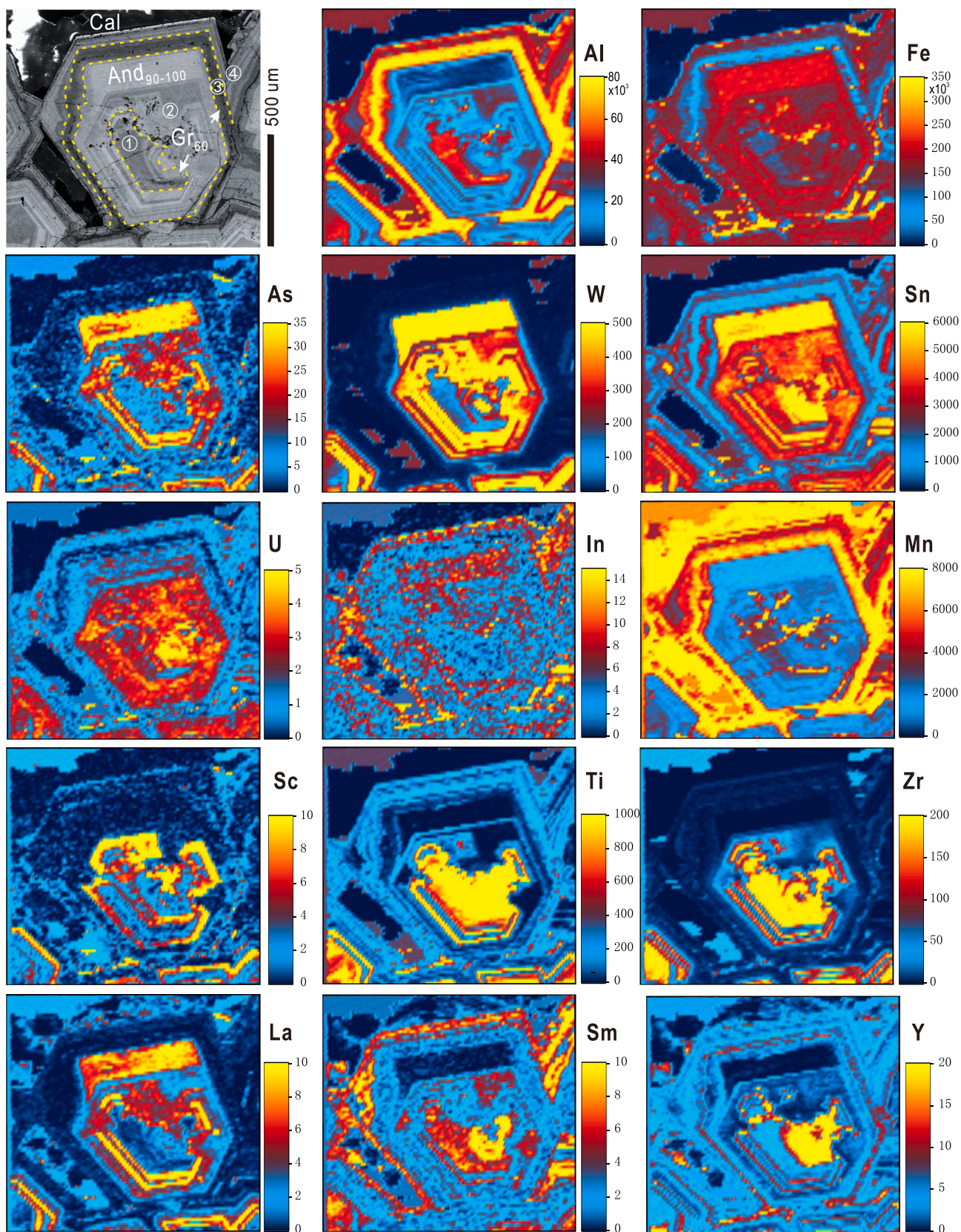


Fig. 8. Laser ablation ICP-MS element maps of oscillatory-zoned garnet from the Lawu deposit showing the distribution of selected elements. Color scales in parts-per-million. The upper left image is a BSE image of the mapped area. Abbreviations: And = andradite; Cal = calcite.

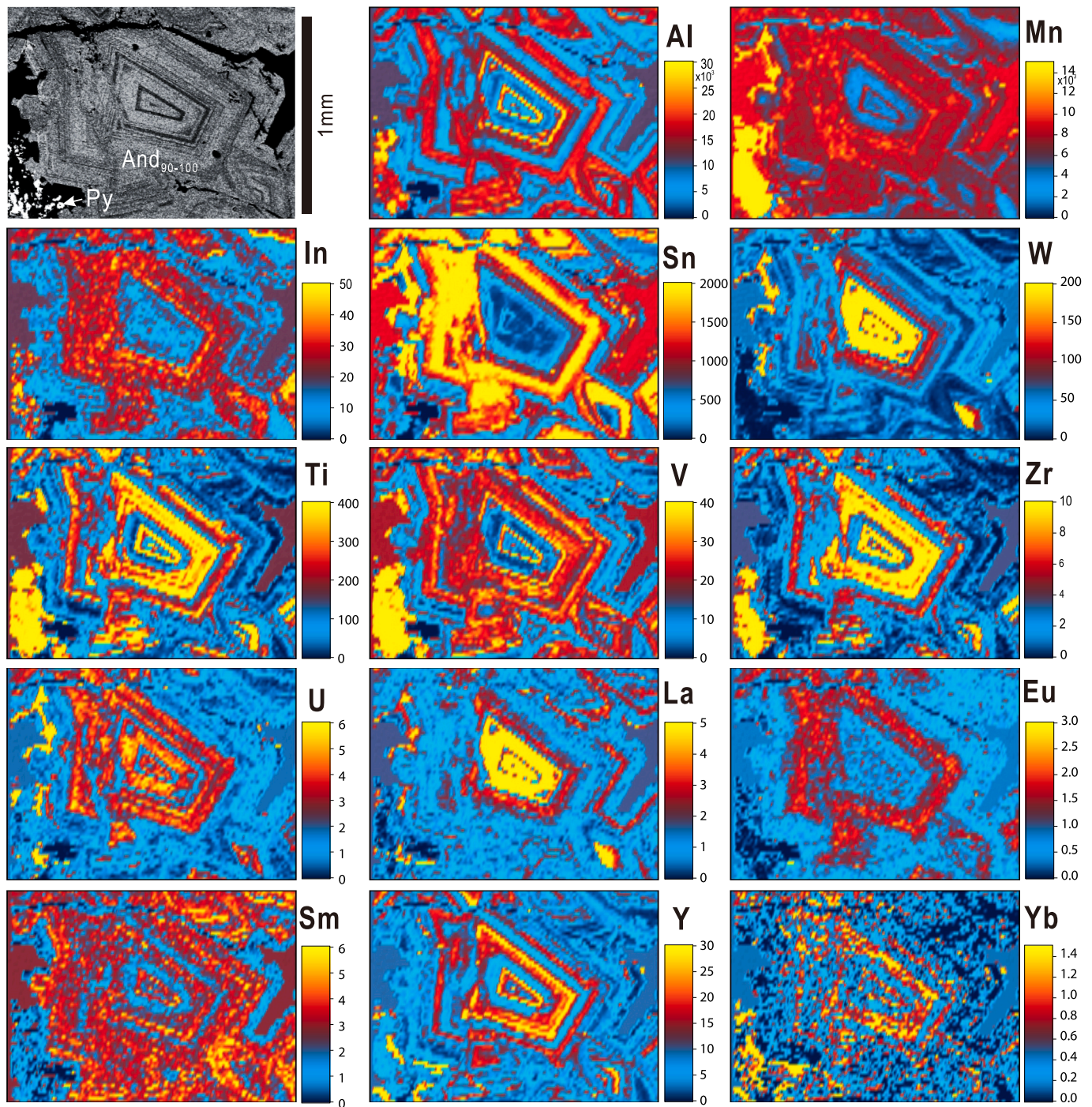


Fig. 9. Laser ablation ICP-MS element maps of oscillatory-zoned garnet from the Yaguila deposit showing the distribution of selected elements. Color scales in parts-per-million. The upper left image is a BSE image of the mapped area. Abbreviations: And = andradite; Py = pyrite.

et al., 2020). Thus, the positive correlation of measured U concentrations with andradite and total REE components at Lawu and Yaguila indicates that U is incorporated into the garnet structure together with REE³⁺ (Fig. 7d, 8 and 9).

In the octahedral coordination of garnet, the radius and/or valence states of U⁴⁺ are comparable to those of HREE, HFSE, and Y (Shannon, 1976), and consequently a positive correlation can be anticipated between U and HREE, HFSE, and Y. However, only weak positive correlations between U and Ti, Zr, Y are noted in the garnets we have analyzed (Figs. 8 and 9). The positive correlation existing between U and total REE in most analyzed garnets (Fig. 7d) is comparable to observations documented previously (Smith et al., 2004; Gasper et al., 2008;

Park et al., 2019). This would infer that incorporation of U into garnet crystals from the hydrothermal fluid is not only governed by equilibrium crystal chemistry, but also by fluid and rock chemistry, such as surface adsorption and occlusion during rapid garnet growth (Smith et al., 2004; Gasper et al., 2008; Deng et al., 2017; Duan et al., 2020).

6.3. Constraints on the timing of Pb–Zn mineralization

To date, only the Re–Os isotope dating of banded pyrrhotite (309 ± 31 Ma) has been conducted to constrain the age of Pb–Zn mineralization in the Lawu deposit (Cui, 2012). This Re–Os age is, however, inconsistent with the whole-rock K–Ar age reported for muscovite monzogranite

Table 1

LA-ICP-MS U–Pb isotopic data for garnets from the Lawu and Yaguila deposits.

sample	Pb (ppm)	Th (ppm)	U (ppm)	Th/U	²⁰⁷ Pb/ ²⁰⁶ Pb	1σ	²⁰⁷ Pb/ ²³⁵ U	1σ	²⁰⁶ Pb/ ²³⁸ U	1σ	²⁰⁸ Pb/ ²³² Th	1σ
LW106, 54.6 ± 2.9 Ma, MSWD = 1.40 (N = 44)												
LW106A4-1	0.08	0.03	1.17	0.03	0.4455	0.0360	1.7057	0.2891	0.0234	0.0015	0.5911	0.0609
LW106A4-2	0.07	0.18	2.12	0.08	0.4007	0.0191	1.0583	0.0886	0.0165	0.0007	0.2054	0.0108
LW106A4-3	0.07	0.54	0.99	0.54	0.5290	0.0295	1.6317	0.1738	0.0241	0.0013	0.0603	0.0029
LW106A4-4	0.09	0.34	1.14	0.29	0.5185	0.0245	2.0670	0.2073	0.0285	0.0013	0.1386	0.0064
LW106A4-5	0.04	0.03	2.88	0.01	0.2140	0.0119	0.3996	0.0309	0.0128	0.0006	0.5800	0.0459
LW106A4-6	0.08	0.26	2.50	0.10	0.3717	0.0164	0.8685	0.0625	0.0168	0.0007	0.1565	0.0072
LW106A4-7	0.23	4.91	2.82	1.74	0.4834	0.0143	1.9529	0.1261	0.0268	0.0010	0.0217	0.0007
LW106A4-8	0.06	0.88	1.61	0.55	0.3792	0.0193	0.8817	0.0698	0.0168	0.0008	0.0308	0.0014
LW106A4-9	0.07	1.68	2.43	0.69	0.3353	0.0144	0.8152	0.0575	0.0168	0.0007	0.0209	0.0009
LW106A4-10	0.08	3.43	2.72	1.26	0.2886	0.0144	0.5411	0.0383	0.0141	0.0006	0.0112	0.0004
LW106A4-11	0.08	3.26	2.67	1.22	0.3048	0.0127	0.7016	0.0481	0.0161	0.0006	0.0112	0.0005
LW106A4-12	0.18	3.79	2.69	1.41	0.4752	0.0144	1.7837	0.1146	0.0246	0.0009	0.0216	0.0007
LW106A4-13	0.11	8.34	2.84	2.94	0.3078	0.0138	0.5968	0.0414	0.0131	0.0006	0.0059	0.0002
LW106A4-14	0.10	2.50	4.49	0.56	0.3047	0.0115	0.6284	0.0392	0.0134	0.0005	0.0185	0.0007
LW106A4-15	0.12	4.22	2.46	1.71	0.3936	0.0142	1.1415	0.0789	0.0196	0.0008	0.0132	0.0005
LW106A4-16	0.10	0.25	1.75	0.14	0.4968	0.0185	1.5906	0.1178	0.0234	0.0010	0.1912	0.0082
LW106A4-17	0.43	0.07	1.58	0.05	0.6568	0.0172	6.2146	0.5508	0.0676	0.0025	2.7876	0.1476
LW106A4-18	0.13	0.03	0.74	0.04	0.6575	0.0303	4.1784	0.5334	0.0459	0.0022	2.1413	0.1813
LW106A4-19	0.20	0.01	0.25	0.02	0.6222	0.0223	16.9723	3.2612	0.1935	0.0087	13.0465	1.8446
LW106A4-20	0.03	0.03	0.21	0.16	0.6060	0.0496	3.9952	0.8712	0.0435	0.0029	0.4037	0.0359
LW106A4-21	0.14	0.02	0.46	0.03	0.7177	0.0402	7.2557	1.4746	0.0795	0.0046	3.9853	0.5423
LW106A4-22	0.54	0.47	1.95	0.24	0.3887	0.0200	0.8849	0.0741	0.0169	0.0008	0.4948	0.0331
LW106A4-23	0.04	0.06	1.23	0.05	0.3553	0.0283	1.0249	0.1408	0.0174	0.0010	0.2571	0.0217
LW106A4-24	0.10	0.02	0.36	0.05	0.6156	0.0327	6.8669	1.3317	0.0755	0.0040	2.6733	0.2975
LW106A1-1	0.15	0.66	1.13	0.59	0.5426	0.0305	1.5795	0.1877	0.0251	0.0013	0.0654	0.0031
LW106A1-2	0.14	0.60	1.21	0.49	0.5543	0.0220	2.6349	0.2579	0.0351	0.0015	0.0880	0.0031
LW106A1-3	0.15	0.66	1.69	0.39	0.5198	0.0198	1.8727	0.1562	0.0270	0.0011	0.0802	0.0029
LW106A1-5	0.13	0.67	1.61	0.42	0.4964	0.0212	1.5924	0.1409	0.0251	0.0011	0.0696	0.0027
LW106A1-6	0.13	0.77	1.63	0.47	0.4572	0.0167	1.8881	0.1504	0.0276	0.0011	0.0637	0.0021
LW106A1-7	0.13	2.42	2.58	0.94	0.4426	0.0149	1.1753	0.0738	0.0193	0.0008	0.0208	0.0006
LW106A1-8	0.30	2.37	2.40	0.99	0.4270	0.0142	1.3973	0.0955	0.0218	0.0009	0.0485	0.0013
LW106A1-9	0.09	0.93	3.45	0.27	0.3492	0.0119	0.7536	0.0444	0.0145	0.0006	0.0382	0.0013
LW106A1-10	0.10	2.34	2.21	1.06	0.3563	0.0143	0.9443	0.0701	0.0183	0.0008	0.0153	0.0006
LW106A1-11	0.29	2.78	2.74	1.01	0.5162	0.0135	2.3820	0.1445	0.0328	0.0012	0.0423	0.0012
LW106A1-14	0.08	3.53	2.70	1.31	0.3264	0.0145	0.6556	0.0463	0.0146	0.0006	0.0098	0.0004
LW106A1-15	0.09	2.25	3.01	0.75	0.3476	0.0168	0.7912	0.0652	0.0147	0.0007	0.0171	0.0008
LW106A1-16	0.12	3.61	2.62	1.38	0.3904	0.0145	1.0070	0.0668	0.0175	0.0007	0.0139	0.0005
LW106A1-17	0.13	2.50	3.12	0.80	0.3757	0.0153	0.9930	0.0742	0.0180	0.0007	0.0207	0.0008
LW106A1-18	0.06	1.58	2.59	0.61	0.2989	0.0152	0.5912	0.0464	0.0133	0.0006	0.0169	0.0007
LW106A1-19	0.10	1.53	2.73	0.56	0.3477	0.0162	0.9587	0.0812	0.0178	0.0008	0.0271	0.0012
LW106A1-21	0.08	1.63	2.63	0.62	0.3854	0.0144	0.8925	0.0587	0.0160	0.0007	0.0229	0.0009
LW106A1-22	0.08	4.58	3.02	1.52	0.3014	0.0127	0.6110	0.0407	0.0139	0.0006	0.0082	0.0003
LW106A1-23	0.08	1.33	2.06	0.65	0.3711	0.0182	0.8900	0.0743	0.0173	0.0008	0.0256	0.0011
LW106A1-24	0.14	4.47	3.11	1.44	0.4045	0.0229	0.8184	0.0775	0.0166	0.0008	0.0148	0.0007
YG51, 68.5 ± 3.4 Ma, MSWD = 0.84 (N = 24)												
YG51-1	0.06	1.12	2.22	0.51	0.2854	0.0142	0.7154	0.0575	0.0170	0.0007	0.0267	0.0011
YG51-2	0.41	0.64	1.77	0.36	0.6518	0.0208	6.8088	0.7416	0.0750	0.0029	0.3142	0.0117
YG51-3	0.36	0.74	1.87	0.40	0.6154	0.0174	3.1110	0.2170	0.0393	0.0015	0.1420	0.0048
YG51-4	0.13	0.78	1.75	0.44	0.5290	0.0171	2.2873	0.1701	0.0320	0.0012	0.0907	0.0032
YG51-5	0.33	0.75	1.17	0.64	0.5968	0.0274	4.2054	0.5715	0.0494	0.0023	0.1421	0.0060
YG51-6	0.09	0.64	1.66	0.38	0.3890	0.0284	1.1638	0.1587	0.0208	0.0012	0.0483	0.0032
YG51-7	0.05	0.79	1.67	0.47	0.1734	0.0188	0.2543	0.0328	0.0127	0.0007	0.0129	0.0011
YG51-8	0.08	0.67	1.15	0.58	0.4589	0.0298	1.9924	0.2746	0.0279	0.0015	0.0631	0.0031
YG51-9	0.03	0.76	1.55	0.49	0.2286	0.0156	0.5613	0.0528	0.0159	0.0007	0.0201	0.0012
YG51-10	0.22	0.83	1.10	0.75	0.5756	0.0244	3.2940	0.3689	0.0418	0.0018	0.0783	0.0032
YG51-11	0.06	0.56	1.62	0.35	0.3781	0.0162	1.1271	0.0866	0.0197	0.0008	0.0490	0.0022
YG51-12	0.04	0.78	1.66	0.47	0.3567	0.0171	0.7943	0.0600	0.0165	0.0007	0.0274	0.0013
YG51-13	0.12	0.05	1.90	0.03	0.2774	0.0174	0.6363	0.0626	0.0172	0.0008	0.5281	0.0417
YG51-14	0.33	0.62	1.04	0.59	0.7273	0.0221	7.6278	0.8131	0.0823	0.0032	0.2636	0.0093
YG51-15	0.36	0.74	1.10	0.68	0.7163	0.0198	5.4127	0.4455	0.0609	0.0023	0.1652	0.0054
YG51-16	0.23	0.45	1.54	0.29	0.6040	0.0170	3.8791	0.2961	0.0479	0.0018	0.2528	0.0087
YG51-17	0.22	0.53	1.74	0.30	0.5513	0.0159	3.3693	0.2563	0.0426	0.0016	0.1988	0.0069
YG51-18	0.12	0.40	1.52	0.26	0.4889	0.0188	2.1257	0.1825	0.0301	0.0012	0.1410	0.0057
YG51-19	0.07	0.54	1.64	0.33	0.4005	0.0209	1.3008	0.1331	0.0208	0.0010	0.0557	0.0030
YG51-20	0.07	0.42	1.91	0.22	0.3667	0.0177	0.9402	0.0756	0.0181	0.0008	0.0778	0.0035
YG51-21	0.12	0.03	3.31	0.01	0.3859	0.0123	1.1540	0.0704	0.0199	0.0008	2.1250	0.1423
YG51-22	0.29	0.87	2.23	0.39	0.3377	0.0145	0.8674	0.0650	0.0182	0.0008	0.0459	0.0019
YG51-23	0.66	1.78	3.02	0.59	0.5166	0.0150	2.1433	0.1404	0.0294	0.0011	0.0706	0.0023
YG51-24	0.07	0.71	2.99	0.24	0.2431	0.0141	0.5076	0.0455	0.0147	0.0007	0.0316	0.0018
YG53, 65.0 ± 4.7 Ma, MSWD = 0.85 (N = 23)												
YG53-1	0.33	0.83	3.67	0.23	0.4938	0.0105	2.5426	0.1261	0.0353	0.0012	0.1885	0.0056
YG53-2	1.04	0.70	3.30	0.21	0.4104	0.0122	1.6473	0.1067	0.0252	0.0009	0.1256	0.0043

(continued on next page)

Table 1 (continued)

sample	Pb (ppm)	Th (ppm)	U (ppm)	Th/U	$^{207}\text{Pb}/^{206}\text{Pb}$	1 σ	$^{207}\text{Pb}/^{235}\text{U}$	1 σ	$^{206}\text{Pb}/^{238}\text{U}$	1 σ	$^{208}\text{Pb}/^{232}\text{Th}$	1 σ
YG53-3	0.17	0.98	4.20	0.23	0.3701	0.0094	1.2003	0.0597	0.0211	0.0008	0.0817	0.0026
YG53-4	0.76	1.03	3.99	0.26	0.5729	0.0101	5.3082	0.2524	0.0617	0.0021	0.3538	0.0100
YG53-5	0.40	0.81	3.71	0.22	0.5137	0.0105	2.8741	0.1432	0.0373	0.0013	0.2361	0.0070
YG53-6	0.26	0.48	3.35	0.14	0.4633	0.0107	2.2655	0.1197	0.0317	0.0011	0.2570	0.0081
YG53-7	0.76	0.78	2.49	0.31	0.6094	0.0124	6.2371	0.3859	0.0701	0.0024	0.3620	0.0108
YG53-8	2.26	0.85	3.39	0.25	0.6415	0.0109	12.6588	0.7322	0.1426	0.0048	1.0012	0.0293
YG53-9	0.16	2.23	2.79	0.80	0.4091	0.0116	1.6376	0.1124	0.0249	0.0009	0.0348	0.0011
YG53-10	0.11	1.50	2.42	0.62	0.4056	0.0127	1.2637	0.0759	0.0223	0.0008	0.0363	0.0012
YG53-11	1.25	1.63	2.98	0.55	0.6623	0.0167	5.3682	0.4179	0.0606	0.0022	0.2157	0.0067
YG53-12	1.03	2.37	4.65	0.51	0.6062	0.0106	5.6901	0.2676	0.0653	0.0022	0.1972	0.0055
YG53-13	0.79	0.68	2.79	0.24	0.6084	0.0110	7.1100	0.3797	0.0849	0.0029	0.5678	0.0165
YG53-15	0.23	1.41	3.96	0.36	0.4364	0.0147	1.4719	0.1033	0.0242	0.0010	0.0667	0.0024
YG53-16	0.50	1.15	2.58	0.45	0.6534	0.0176	4.6252	0.3702	0.0541	0.0020	0.2857	0.0091
YG53-17	0.78	0.68	2.63	0.26	0.6121	0.0144	6.4487	0.5056	0.0732	0.0026	0.4273	0.0139
YG53-18	1.29	1.14	2.95	0.39	0.6474	0.0142	7.7506	0.5893	0.0950	0.0034	0.4348	0.0136
YG53-19	0.51	1.09	3.18	0.34	0.5809	0.0115	4.5360	0.2431	0.0513	0.0018	0.2363	0.0069
YG53-20	1.52	1.91	2.86	0.67	0.5997	0.0131	6.4184	0.4581	0.0725	0.0026	0.1853	0.0055
YG53-21	0.16	1.20	3.83	0.31	0.3628	0.0169	1.2830	0.1253	0.0231	0.0010	0.0659	0.0030
YG53-22	0.12	1.33	4.29	0.31	0.2944	0.0097	0.6794	0.0382	0.0167	0.0006	0.0413	0.0015
YG53-23	0.50	1.74	3.87	0.45	0.5349	0.0160	2.0475	0.1412	0.0297	0.0011	0.1041	0.0035
YG53-24	0.49	1.22	3.15	0.39	0.5236	0.0122	2.0765	0.1068	0.0311	0.0011	0.2073	0.0060

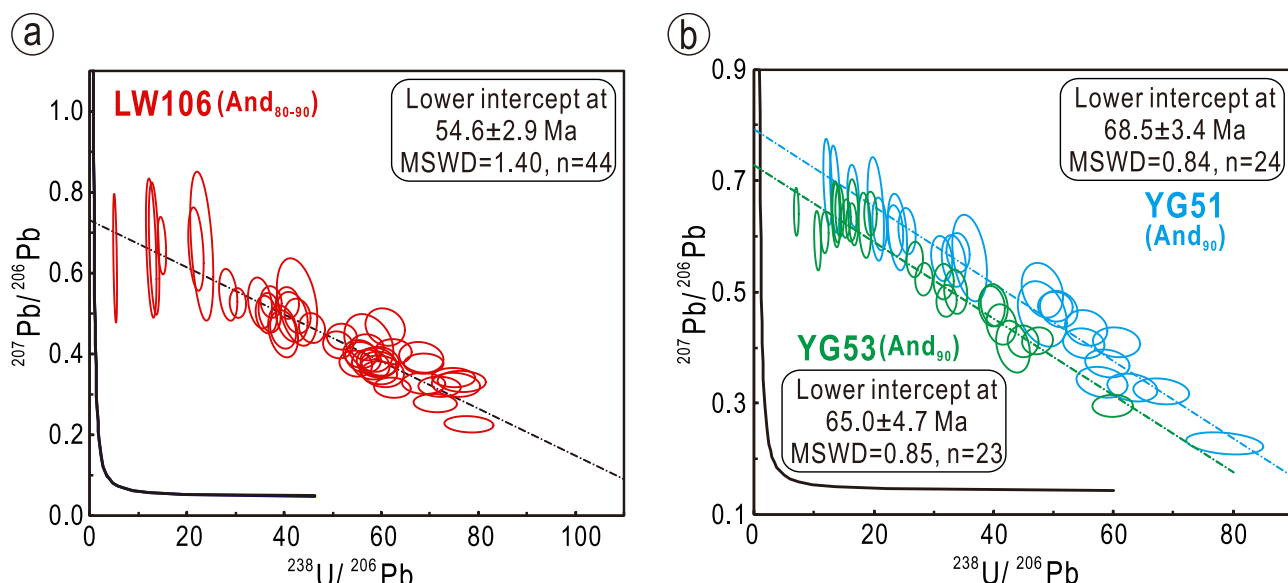


Fig. 10. Tera-Wasserburg U–Pb concordia diagrams of garnets from the Lawu (a) and Yaguila (b) deposits.

(109 ± 1.3 Ma; Du et al., 2004) and, in consequence, a multi-stage sedimentary exhalative style of mineralization has been proposed (Du et al., 2004; Cui, 2012). The formation age of the Yaguila Pb–Zn skarn deposit was poorly understood due to the multiple magmatic pulses in the mining area (Huang et al., 2012; Zhao et al., 2016; Gao et al., 2017; Xu et al., 2019). It is tempting to link different igneous rocks to discrete types of mineralization (skarn-type Pb–Zn and porphyry-type Mo), or ore stages, merely through the contact relationships between rhyolitic volcanic rocks and Pb–Zn skarns, as well as the molybdenite Re–Os ages of porphyry Mo mineralization (Huang et al., 2012; Gao et al., 2017).

In this study, homogeneous domains in prograde garnets with relatively high U contents were selected for LA–ICP–MS U–Pb geochronology, yielding U–Pb ages of 54.6 ± 2.9 Ma (MSWD = 1.4, N = 44) for the Lawu skarn, and two overlapping ages 68.5 ± 3.4 Ma (MSWD = 0.84, N = 24) and 65.0 ± 4.7 Ma (MSWD = 0.85, N = 23) for the Yaguila skarn. Textural relationships and mineral associations in both deposits suggest that Pb–Zn skarn mineralization belongs to the sulfide stage and that garnet U–Pb ages represent the lower age limit of the ore formation.

The new garnet U–Pb age for Pb–Zn mineralization in the Lawu

deposit is not concordant with either the pyrrhotite Re–Os age (309 ± 31 Ma) of quartz-sulfide veins given by Cui (2012) or the whole-rock K–Ar age (109 ± 1.3 Ma) of muscovite monzogranite (Du et al., 2004). This discrepancy excludes the possibility of a sedimentary exhalative origin for the Pb–Zn ores as well as any genetic link between muscovite monzogranite and mineralization. Rather, a causative intrusion not exposed in the mine is a more plausible explanation, also noting that the mineralization may be distal to the hidden intrusion. For the Yaguila deposit, the newly obtained garnet U–Pb ages are, within analytical error, in agreement with published zircon U–Pb ages of Paleocene quartz porphyry (~ 65 Ma; Xu et al., 2019), an exposed dyke surrounded by porphyry Mo mineralization (quartz-molybdenite veins in porphyry and slate) with molybdenite Re–Os ages of 65.0 ± 1.9 Ma (Gao et al., 2017). This provides new geochronological evidence for the synchronicity of skarn-type Pb–Zn and porphyry-type Mo mineralization as well as their genetic association with the Paleocene quartz porphyry.

A series of Pb–Zn skarn deposits are reported in the east and central section of the Nyainqentanglha metallogenic belt (Fig. 1b). Integrating the new ages with published age constraints (Fig. 11), the abundant

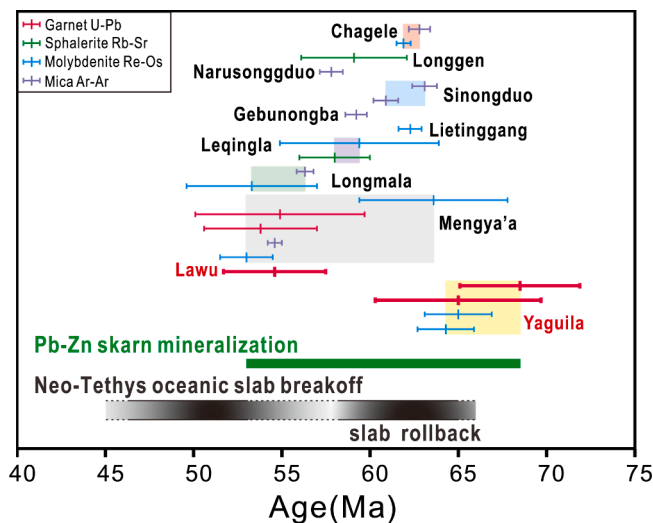


Fig. 11. Summary plot showing the age constraints for the major Pb–Zn skarn deposits in the Nyainqentanglha metallogenic belt. Mineralization ages are from Huang et al. (2012); Ji et al. (2014); Yang et al. (2014); Fu et al. (2015); Wang et al. (2015); Gao et al. (2017); Xu et al. (2019); Gao et al. (2019); Gao et al. (2020); Gao et al. (2021); Li et al. (2019a); Ma et al. (2020); Jiang et al. (2021). Data in this study are shown in red bold lines, and those from other deposits are framed in semi-transparent boxes with different colors.

Pb–Zn skarn deposits in this belt formed during the Paleocene (~65 Ma) to the early Eocene (~53 Ma). We consider metallogenesis as a large-scale magmatic-hydrothermal event triggered by partial melting of middle-upper crustal source material following slab rollback (from ~65 Ma) and slab breakoff (from ~53 Ma) of the Neo-Tethys Ocean and subsequent asthenosphere upwelling during the main stage of the India–Asia continental collision (~65–41 Ma; Zheng et al., 2015b; Deng et al., 2022).

6.4. A potential geochronometer for Pb–Zn skarn systems

Confirming the age of Pb–Zn skarn mineralization by radiometric dating of ore minerals (sphalerite and galena), associated minerals, and intrusive rocks interpreted to be involved in ore genesis, remains challenging for three reasons. Firstly, Pb–Zn sulfides generally have poor isotopic retentivity and associated minerals (e.g., K-bearing minerals, U-bearing accessories and other sulfides) are not commonly observed. Secondly, Pb–Zn skarn mineralization often occurs distal to igneous rocks without an unequivocal causative intrusion (e.g., Mengya'a Pb–Zn deposit, Jiang et al., 2021). Lastly, evidence for complex multistage ore-forming processes involving multiple magmatic phases and diverse mineralization types is common in Pb–Zn skarns in Tibet and elsewhere (Sillitoe, 2010; Gao et al., 2021). Therefore, only a few reliable Pb–Zn mineralization ages have been reported, making new ways to understand the temporal and genetic relationships between magmatism and mineralization a fertile research field.

Garnet is a ubiquitous skarn mineral in various economic ore deposits, and typically containing negligible common Pb. The occurrence of U in garnet with different compositions (e.g., grandite, spessartine and schorlomite) has been widely studied and shown to be lattice-bound (Deng et al., 2017; Seman et al., 2017; Li et al., 2018; Yang et al., 2018; Jiang et al., 2021), making it amenable for U–Pb dating of mineralization. Although it has been shown that garnets with as little as ~1 ppm U can yield precise U–Pb age (Wafforn et al., 2018), detailed investigation of the content and distribution of U in garnet is still necessary prior to U–Pb analysis. Our study suggests that the high U abundance in grandite is generally coupled with andradite-rich zones, coincident with previous findings that texturally homogeneous andradite-rich domains in grandite tend to increase the likelihood of obtaining a high precision garnet

U–Pb age (Seman et al., 2017; Gevedon et al., 2018; Duan et al., 2020; Reinhardt et al., 2022).

Currently, successful applications of U–Pb dating have been reported in calcic garnets from Fe, Cu, Au, W, Mo, Sn skarn deposits and gold vein deposits. These include examples in China (e.g., Nanminghe Fe skarn in North China craton, Deng et al., 2017; Mengku Fe skarn in Chinese Altai, Zang et al., 2019; Yinan Au–Cu skarn in North China craton, Duan et al., 2020; Dongping Au–Te vein in North China craton, Fan et al., 2021; and Zhuxi W–Cu skarn in South China, Hong et al., 2022). Examples outside China include the Big Gossan Cu skarn (East Indonesia, Wafforn et al., 2018), the Darwin W skarn (North American Cordillera, Gevedon et al., 2018), and Sn, W, Fe, Zn, Cu, and In skarns in the Erzgebirge, Germany (Burisch et al., 2019; Reinhardt et al., 2022). Furthermore, U–Pb dating of spessartine-rich (Li et al., 2018), Ti-bearing (Jiang et al., 2021), and grandite garnets (Li et al. (2019a); Hong et al., 2021; Sun et al., 2022; Wen et al., 2022) have been applied in skarn-type and sediment-hosted Pb–Zn deposits. This growing volume of research notwithstanding, garnet U–Pb geochronology remains underutilized as a method for accurate dating of Pb–Zn skarn systems despite the common presence of U-bearing garnet from Pb–Zn skarns. The successful in-situ LA–ICP–MS U–Pb dating in our study highlights the value of skarn garnet for providing accurate constraints on mineralization age in complex terranes.

7. Conclusions

Skarn garnet is recognized in association with Pb–Zn mineralization and generally contains measurable concentrations of structure-bound U (0.07–5.3 ppm) in the Lawu and Yaguila Pb–Zn deposits, providing a new approach to constrain mineralization age. LA–ICP–MS U–Pb geochronology of garnets from the two deposits yield U–Pb dates of 54.6 ± 2.9 Ma and 65.0 ± 4.7 to 68.5 ± 3.4 Ma, respectively. These garnet U–Pb dates provide precise constraints on the timing of Pb–Zn mineralization and reveal the magmatic-hydrothermal origin of Pb–Zn skarn mineralization in the Nyainqentanglha metallogenic belt, disproving the sedimentary exhalative origin proposed previously. Combined with existing radiometric age data, the results presented here suggest that the district-wide Pb–Zn skarn mineralization in the Nyainqentanglha metallogenic belt is associated with voluminous magmatism caused by slab rollback and breakoff of the Neo-Tethys Ocean during the India–Asia continental collision. Our study highlights the feasibility, and thus the potential, of garnet as a U–Pb geochronometer for Pb–Zn skarn systems.

8. Funding information

National Natural Science Foundation of China (41802098, 42230807).

Declaration of Competing Interest

The authors declare that they have no known competing financial interests or personal relationships that could have appeared to influence the work reported in this paper.

Data availability

Data for this article are shared in the [Supplementary Material](#).

Acknowledgements

We thank Adelaide Microscopy staff for assistance with microanalytical work. The constructive and insightful comments of three anonymous reviewers helped us improve presentation of our results.

Appendix A. Supplementary data

Supplementary data to this article can be found online at <https://doi.org/10.1016/j.oregeorev.2023.105565>.

References

- Bau, M., 1991. Rare-earth element mobility during hydrothermal and metamorphic fluid-rock interaction and the significance of the oxidation state of europium. *Chem. Geol.* 93 (3–4), 219–230.
- Burisch, M., Gerdes, A., Meinert, L.D., Albert, R., Seifert, T., Gutzmer, J., 2019. The essence of time-fertile skarn formation in the Variscan Orogenic Belt. *Earth Planet. Sc. Lett.* 519, 165–170.
- Cao, M., Qin, K., Evans, N.J., Li, G., Ling, X., McInnes, B.I.A., Zhao, J., 2021. Titanite in situ SIMS U-Pb geochronology, elemental and Nd isotopic signatures record mineralization and fluid characteristics at the Pusanguo skarn deposit, Tibet. *Miner. Deposita* 56 (5), 907–916.
- Cui, Y.B., 2012. Geological-geochemical characteristics and genesis of Lawu zinc-copper polymetallic ore deposit in Tibet. *China Univ. of Geosci. (Beijing)* p17, 32.
- Deng, X.D., Li, J.W., Luo, T., Wang, H.Q., 2017. Dating magmatic and hydrothermal processes using andradite-rich garnet U-Pb geochronometry. *Contrib. Mineral. Petr.* 172, 1–11.
- Deng, X.-H., Wang, J.-B., Pirajno, F., Wang, Y.-W., Li, Y.-C., Li, C., Zhou, L.-M., Chen, Y.-J., 2016. Re-Os dating of chalcopyrite from selected mineral deposits in the Kalatag district in the eastern Tianshan Orogen. *China. Ore Geol. Rev.* 77, 72–81.
- Deng, J., Wang, Q., Sun, X., Yang, L., Groves, D.I., Shu, Q., Gao, L., Yang, L., Qiu, K., Wang, C., Dong, C., 2022. Tibetan ore deposits: A conjunction of accretionary orogeny and continental collision. *Earth-Sci. Rev.* 235, 104245.
- Dhiyva, L., Janani, N., Palanivel, B., Murugan, R., 2013. Li^+ transport properties of W substituted $\text{Li}_7\text{La}_3\text{Zr}_2\text{O}_{12}$ cubic lithium garnets. *AIP Advances* 3(8), 082115.
- Du, X., Liu, J.T., Wang, Y.P., 2004. Geological character and ore genesis of the Lawu copper-lead-zinc polymetallic ore deposit. *Mineral Resour. Geol.* 18 (5), 410–414 in Chinese with English abstract.
- Duan, Z., Gleeson, S.A., Gao, W.-S., Wang, F.-Y., Li, C.-J., Li, J.-W., 2020. Garnet U-Pb dating of the Yinan Au-Cu skarn deposit, Luxi district, North China Craton: Implications for district-wide coeval Au-Cu and Fe skarn mineralization. *Ore Geol. Rev.* 118, 103310.
- Fan, G.H., Li, J.W., Deng, X.D., Gao, W.S., Li, S.Y., 2021. Age and origin of the Dongping Au-Te deposit in the North China Craton revisited: evidence from paragenesis, geochemistry, and in situ U-Pb geochronology of garnet. *Econ. Geol.* 116 (4), 963–985.
- Fu, Q., Huang, K.X., Zheng, Y.C., Yang, Z.S., Duan, L.F., 2015. Ar-Ar age of muscovite from skarn orebody of the Mengya'a lead-zinc deposit in Tibet and its geodynamic significance. *Acta Geol. Sin.* 89 (3), 569–582 in Chinese with English abstract.
- Gao, S., Zheng, Y., Jiang, J., Tian, K., Xu, J., 2019. Geochemistry and geochronology of the Gebunongba iron polymetallic deposit in the Gangdese Belt. *Tibet. J. Earth Sci.* 30 (2), 296–308.
- Gao, S., Chen, X., Cheng, S., Zhang, Y., Zheng, Y., Jiang, J., Wu, S., Jiang, X., 2020. Syn-collisional magmatism at the Longgen Pb-Zn deposit, western Nyainqentanglha belt, Tibet: Petrogenesis and implications for regional polymetallic metallogeny. *Ore Geol. Rev.* 126, 103730.
- Gao, S., Chen, X., Zhang, Y., Zheng, Y., Long, T., Wu, S., Jiang, X., 2021. Timing and genetic link of porphyry Mo and skarn Pb-Zn mineralization in the Chagele deposit, Western Nyainqentanglha belt. *Tibet. Ore Geol. Rev.* 129, 103929.
- Gao, Y.M., Lan, Z.W., Chen, Y.C., Tang, J.X., 2017. Geochronological and geochemical constraints on the origin of Yagula Cretaceous and Palaeogene ore-bearing quartz porphyries, Central Lhasa Terrane. *Tibet. Geol. J.* 52 (1), 45–66.
- Gaspar, M., Knaack, C., Meinert, L.D., Moretti, R., 2008. REE in skarn systems: a LA-ICP-MS study of garnets from the crown jewel gold deposit. *Geochim. Cosmochim. Acta* 72 (1), 185–205.
- Gevedon, M., Seman, S., Barnes, J.D., Lackey, J.S., Stockli, D.F., 2018. Unraveling histories of hydrothermal systems via U-Pb laser ablation dating of skarn garnet. *Earth Planet. Sc. Lett.* 498, 237–246.
- Guo, X., Navrotsky, A., Kukkadapu, R.K., Engelhard, M.H., Lanzirrotti, A., Newville, M., Ilton, E.S., Sutton, S.R., Xu, H., 2016. Structure and thermodynamics of uranium containing iron garnets. *Geochim. Cosmochim. Acta* 189, 269–281.
- Hnatyshin, D., Creaser, R.A., Meffre, S., Stern, R.A., Wilkinson, J.J., Turner, E.C., 2020. Understanding the microscale spatial distribution and mineralogical residency of Re in pyrite: Examples from carbonate-hosted Zn-Pb ores and implications for pyrite Re-Os geochronology. *Chem. Geol.* 533, 119427.
- Hong, J., Zhang, H., Zhai, D., Li, D., Zhang, Y., Liu, J., 2021. The geochronology of the Haobugao skarn Zn-Pb deposit (NE China) using garnet LA-ICP-MS U-Pb dating. *Ore Geol. Rev.* 139, 104437.
- Hong, J., Zhang, H., Li, D., Ouyang, Y., Zhai, D., Liu, F., Liu, J., 2022. In situ LA-ICP-MS U-Pb geochronology and geochemical characteristics of garnet from the Zhuxi skarn W-Cu deposit. *South China. Ore Geol. Rev.* 140, 104577.
- Hou, Z.-Q., Gao, Y.-F., Qu, X.-M., Rui, Z.-Y., Mo, X.-X., 2004. Origin of adakitic intrusives generated during mid-Miocene east-west extension in southern Tibet. *Earth Planet. Sc. Lett.* 220 (1–2), 139–155.
- Huang, K.X., Zheng, Y.Y., Zhang, S., Li, W., Sun, Q., Li, Q., Hou, Z.Q., 2012. LA-ICP-MS zircon U-Pb dating of two types of porphyry in the Yagula mining area. *Tibet. Acta Petro. Miner.* 31 (3), 348–360 in Chinese with English abstract.
- Jamtveit, B., Wogelius, R.A., Fraser, D.G., 1993. Zonation patterns of skarn garnets: Records of hydrothermal system evolution. *Geology* 21 (2), 113–116.
- Ji, X.H., Meng, X.J., Yang, Z.S., Zhang, Q., Tian, S.H., Li, Z.Q., Liu, Y.C., Yu, Y.S., 2014. The Ar-Ar geochronology of sericite from the cryptoexplosive breccia type Pb-Zn deposit in Narusongduo, Tibet and its geological significance. *Geol. Explor.* 50 (2), 0281–0290 in Chinese with English abstract.
- Ji, W.-Q., Wu, F.-Y., Chung, S.-L., Li, J.-X., Liu, C.-Z., 2009. Zircon U-Pb geochronology and Hf isotopic constraints on petrogenesis of the Gangdese batholith, southern Tibet. *Chem. Geol.* 262 (3–4), 229–245.
- Jiang, X., Zheng, Y., Gao, S., Yan, J., Kang, Y., Jiang, G., Liu, J., Zhang, Z., Chen, X., 2021. In-situ U-Pb geochronology of Ti-bearing andradite as a practical tool for linking skarn alteration and Pb-Zn mineralization: a case study of the Mengya'a deposit. *Tibet. Ore Geol. Rev.* 139, 104565.
- Jochum, K.L., Weis, U., Schwager, B., Stoll, B., Wilson, S.A., Haug, G.H., Andreea, M.O., Enzweiler, J., 2016. Reference values following ISO guidelines for frequently requested rock reference materials. *Geostand. Geoanal. Res.* 40 (3), 333–350.
- Keankeo, W., Hermann, J., 2002. The oscillatory intergrowth of feldspars in titanite and andradite, Little Dromedary, NSW, Australia. *Eur. J. Mineral.* 14 (2), 379–388.
- Li, D.F., Fu, Y., Sun, X.M., 2018. Onset and duration of Zn-Pb mineralization in the Talate Pb-Zn (Fe) skarn deposit, NW China: constraints from spessartine U-Pb dating. *Gondwana Res.* 63, 117–128.
- Li, D.F., Tan, C.Y., Miao, F.Y., Liu, Q.F., Zhang, Y., Sun, X.M., 2019a. Initiation of Zn-Pb mineralization in the Pingbao Pb-Zn skarn district, South China: Constraints from U-Pb dating of grossular-rich garnet. *Ore Geol. Rev.* 107, 587–599.
- Li, H.F., Tang, J.X., Hu, G.Y., Ding, S., Li, Z., Xie, F.W., Teng, L., Cui, S.Y., 2019b. Fluid inclusions, isotopic characteristics and geochronology of the Sinongduo epithermal Ag-Pb-Zn deposit, Tibet, China. *Ore Geol. Rev.* 107, 692–706.
- Liu, X.J., Liu, W., Liu, L.J., 2012. The generation of a stratiform skarn and volcanic exhalative Pb-Zn deposit (Sawusi) in the southern Chinese Altay Mountains: the constraints from petrography, mineral assemblage and chemistry. *Gondwana Res.* 22 (2), 597–614.
- Liu, Y., Qi, L., Gao, J., Ye, L., Huang, Z., Zhou, J., 2015. Re-Os dating of galena and sphalerite from lead-zinc sulfide deposits in Yunnan Province. *SW China. J. Earth Sci.* 26 (3), 343–351.
- Liu, J.M., Shen, J., 1998. The method and significance of isotopic dates for metal deposits. *Geol. Explor. Non-Ferrous Met.* 7 (2), 107–113 in Chinese.
- Ludwig, K.R., 2003. *User's Manual for Isoplot 3.00. A Geochronological Toolkit for Microsoft Excel. Special Publication No. 4a. Berkeley Geochronology Center, Berkeley, California, p. 70.*
- Ma, W., Liu, Y.C., Liu, Y.C., Yang, Z.S., Li, Z.Q., Zhao, X.Y., Yue, L.L., Tang, B.L., 2020. Sulfide Re-Os and Rb-Sr ages of Lietingang-Leqingla Pb-Zn-Fe-Cu-Mo deposit in Tibet and its geological significance. *Miner. Deposits* 39 (1), 80–96 in Chinese with English abstract.
- McDonough, W.F., Sun, S.S., 1995. The composition of the Earth. *Chem. Geol.* 120 (3–4), 223–253.
- Mezger, K., Hanson, G.N., Bohlen, S.R., 1989. U-Pb systematics of garnet: dating the growth of garnet in the Late Archean Pikwitonei granulite domain at Cauchon and Nativahunan Lakes, Manitoba, Canada. *Contrib. Mineral. Petr.* 101 (2), 136–148.
- Milenkov, G., Vassileva, R., Georgieva, S., Grozdev, V., Peytcheva, I., 2022. Trace-element signatures and U-Pb geochronology of magmatic and hydrothermal titanites from the Petrovitsa Pb-Zn deposit, Madan region, Central Rhodopes (Bulgaria). *Geol. Balc.* 51 (2), 79–91.
- Mo, X., Niu, Y., Dong, G., Zhao, Z., Hou, Z., Zhou, S., Ke, S., 2008. Contribution of syn-collisional felsic magmatism to continental crust growth: a case study of the Paleogene Linzizong volcanic succession in southern Tibet. *Chem. Geol.* 250 (1–4), 49–67.
- Nakai, S.I., Halliday, A.N., Kesler, S.E., Jones, H.D., 1990. Rb-Sr dating of sphalerites from Tennessee and the genesis of Mississippi Valley type ore deposits. *Nature* 346 (6282), 354–357.
- Ostendorf, J., Henjes-Kunst, F., Schneider, J., Melcher, F., Gutzmer, J., 2017. Genesis of the carbonate-hosted Tres Marias Zn-Pb-(Ge) deposit, Mexico: constraints from Rb-Sr sphalerite geochronology and Pb isotopes. *Econ. Geol.* 112 (5), 1075–1087.
- Park, C., Park, C., Song, Y., Choi, S.-G., 2019. Sequential trace element analysis of zoned skarn garnet: implications for multi-stage fluxing and flow of magmatic fluid into a skarn system. *Lithos* 350–351, 105213.
- Paton, C., Hellstrom, J., Paul, B., Woodhead, J., Hergt, J., 2011. Iolite: Freeware for the visualisation and processing of mass spectrometric data. *J. Anal. Atom. Spec.* 26, 2508–2518.
- Pearce, N.J.G., Perkins, W.T., Westgate, J.A., Gorton, M.P., Jackson, S.E., Neal, C.R., Chenery, S.P., 1997. A compilation of new and published major and trace element data for NIST SRM 610 and NIST SRM 612 glass reference materials. *Geostand. Newslett.* 21 (1), 115–144.
- Rák, Z., Ewing, R.C., Becker, U., 2011. Role of iron in the incorporation of uranium in ferric garnet matrices. *Phys. Rev. B* 84 (15), 155128.
- Reinhardt, N., Gerdes, A., Beranoguirre, A., Frenzel, M., Meinert, L.D., Gutzmer, J., Burisch, M., 2022. Timing of magmatic-hydrothermal activity in the Variscan Orogenic Belt: LA-ICP-MS U-Pb geochronology of skarn-related garnet from the Schwarzenberg District. *Erzgebirge. Miner. Deposita* 57 (6), 1071–1087.
- Seman, S., Stockli, D.F., McLean, N.M., 2017. U-Pb geochronology of grossular-andradite garnet. *Chem. Geol.* 460, 106–116.
- Shannon, R.D., 1976. Revised effective ionic radii and systematic studies of interatomic distances in halides and chalcogenides. *Acta Crystallogr. A* 32 (5), 751–767.
- Sillitoe, R.H., 2010. Porphyry copper systems. *Econ. Geol.* 105 (1), 3–41.
- Smith, M.P., Henderson, P., Jeffries, T.E.R., Long, J., Williams, C.T., 2004. The rare earth elements and uranium in garnets from the Beinn Dubhaich Aureole, Skye, Scotland, UK: constraints on processes in a dynamic hydrothermal system. *J. Petrol.* 45, 457–484.

- Sun, C., Yang, X., Zhang, H., Ji, W., Chen, B.o., Dong, Z., Faisal, M., Xi, D., 2022. Tracing the formation and modification of the Keketale VMS-type Pb–Zn deposit, Altai Mountains: Insights from ore deposit geology, geochronology, and magnetite geochemistry. *Ore Geol. Rev.* 144, 104852.
- Sverjensky, D.A., 1984. Europium redox equilibria in aqueous solution. *Earth Planet. Sc. Lett.* 67 (1), 70–78.
- Tera, F., Wasserburg, G.J., 1972. U–Th–Pb systematics in three Apollo 14 basalts and the problem of initial Pb in lunar rocks. *Earth Planet. Sc. Lett.* 14 (3), 281–304.
- Van Achterbergh, E., Ryan, C.G., Jackson, S.E., Griffin, W.L. 2001. Data reduction software for LAICP-MS. In: Sylvester, J.P. (Ed.), *Laser-ablation-ICPMS in the Earth Sciences; Principles and Applications*. Mineralogical Association of Canada, Short Course Series 29, 239–243.
- van Westrenen, W., Allan, N.L., Blundy, J.D., Purton, J.A., Wood, B.J., 2000. Atomistic simulation of trace element incorporation into garnets-comparison with experimental garnet-melt partitioning data. *Geochim. Cosmochim. Ac.* 64 (9), 1629–1639.
- Wafforn, S., Seman, S., Kyle, J.R., Stockli, D., Leys, C., Sonbait, D., Cloos, M., 2018. Andradite garnet U–Pb geochronology of the Big Gossan skarn, Ertzberg-Grasberg mining district. Indonesia. *Econ. Geol.* 113 (3), 769–778.
- Wang, Y.C., Duan, D.F., 2021. REE Distribution Character in Skarn Garnet and Its Geological Implication. *Acta Sci. Nat. Univ. Pek.* 57 (3), 446–458 in Chinese with English abstract.
- Wang, L.Q., Tang, J.X., Deng, J., Kang, H.R., Lin, X., Cheng, W.B., Li, Z., Zhang, Z., 2015. The Longmala and Mengya'a skarn Pb–Zn deposits, Gangdese region, Tibet: evidence from U–Pb and Re–Os geochronology for formation during early India–Asia collision. *Int. Geol. Rev.* 57 (14), 1825–1842.
- Wen, B., Zhang, Y.H., Yang, W.Z., Du, S.Z., Wang, P., Liu, J.W., Chen, L., 2022. U–Pb Geochronology and geochemistry of stratiform Garnet from the Aqishan Pb–Zn Deposit, Eastern Tianshan, Xinjiang, NW China: Constraints on genesis of the deposit. *Acta Geol. Sin.* 96 (1), 135–146.
- Wu, S., Wörner, G., Jochum, K.P., Stoll, B., Simon, K., Kronz, A., 2019. The preparation and preliminary characterisation of three synthetic andesite reference glass materials (ARM-1, ARM-2, ARM-3) for in situ microanalysis. *Geostand. Geoanal. Res.* 43 (4), 567–584.
- Wu, S., Yang, M., Yang, Y., Xie, L., Huang, C., Wang, H., Yang, J., 2020. Improved in situ zircon U–Pb dating at high spatial resolution (5–16 μm) by laser ablation-single collector-sector field-ICP-MS using Jet sample and X skimmer cones. *Int. J. Mass Spectrom.* 456, 116394.
- Wu, S., Yang, Y., Jochum, K.P., Romer, R.L., Glodny, J., Savov, I.P., Agostini, S., De Hoog, J.C.M., Peters, S.T.M., Kronz, A., Zhang, C., Bao, Z., Wang, X., Li, Y., Tang, G., Feng, L., Yu, H., Li, Z., Zhang, L.e., Lin, J., Zeng, Y., Xu, C., Wang, Y., Cui, Z., Deng, L. i., Xiao, J., Liu, Y., Xue, D., Zhang, D.i., Jia, L., Wang, H., Xu, L., Huang, C., Xie, L., Pack, A., Wörner, G., He, M., Li, C., Yuan, H., Huang, F., Li, Q., Yang, J., Li, X., Wu, F., 2021. Isotopic compositions (Li–B–Si–O–Mg–Sr–Nd–Hf–Pb) and $\text{Fe}^{2+}/\Sigma\text{Fe}$ ratios of three synthetic andesite glass reference materials (ARM-1, ARM-2, ARM-3). *Geostand. Geoanal. Res.* 45 (4), 719–745.
- Xu, J., Ciobanu, C.L., Cook, N.J., Zheng, Y.Y., Sun, X., Wade, B.P., 2016. Skarn formation and trace elements in garnet and associated minerals from Zhibula copper deposit, Gangdese Belt, southern Tibet. *Lithos* 262, 213–231.
- Xu, J., Zheng, Y.Y., Sun, X., Li, X.F., Mao, G.Z., 2019. Genesis of the Yaguila Pb–Zn–Ag–Mo skarn deposit in Tibet: Insights from geochronology, geochemistry, and fluid inclusions. *J. Asian Earth Sci.* 172, 83–100.
- Xu, J., Ciobanu, C.L., Cook, N.J., Zheng, Y.Y., Li, X.F., Wade, B.P., Verdugo-Ihl, M.R., Gao, W.Y., Zhu, Q.Q., 2020. Numerical modelling of rare earth element fractionation trends in garnet: a tool to monitor skarn evolution. *Contrib. Mineral. Petr.* 175 (4), 30.
- Yang, Y., Duo, J., Liu, H.F., Zhang, J.S., Wang, L.Q., Zhang, Z., Hu, Z.H., 2014. Re–Os dating of molybdenite from the Lietinggang iron polymetallic deposit of Tibet and its geological significance. *Geol. China* 41 (5), 1554–1564 in Chinese with English abstract.
- Yang, Y.H., Wu, F.Y., Yang, J.H., Mitchell, R.H., Zhao, Z.F., Xie, L.W., Huang, C., Ma, Q., Yang, M., Zhao, H., 2018. U–Pb age determination of schorlomite garnet by laser ablation inductively coupled plasma mass spectrometry. *J. Anal. Atom. Spectrom.* 33 (2), 231–239.
- Yardley, B.W.D., Rochelle, C.A., Barnicoat, A.C., Lloyd, G.E., 1991. Oscillatory zoning in metamorphic minerals: An indicator of infiltration metasomatism. *Mineral. Mag.* 55 (380), 357–365.
- Yin, A., Harrison, T.M., 2000. Geologic evolution of the Himalayan–Tibetan Orogen. *Annu. Rev. Earth Pl. Sc.* 28 (1), 211–280.
- Zang, Z.J., Dong, L.L., Liu, W., Zhao, H., Wang, X.S., Cai, K.D., Wan, B., 2019. Garnet U–Pb and O isotopic determinations reveal a shear-zone induced hydrothermal system. *Sci. Rep.* 9 (1), 10382.
- Zhao, J.X., Li, G.M., Evans, N.J., Qin, K.Z., Li, J.X., Zhang, X.N., 2016. Petrogenesis of Paleocene–Eocene porphyry deposit-related granitic rocks in the Yaguila–Sharang ore district, central Lhasa terrane. Tibet. *J. Asian Earth Sci.* 129, 38–53.
- Zheng, Y.C., Fu, Q., Hou, Z.Q., Yang, Z.S., Huang, K.X., Wu, C.D., Sun, Q.Z., 2015b. Metallogeny of the northeastern Gangdese Pb–Zn–Ag–Fe–Mo–W polymetallic belt in the Lhasa terrane, southern Tibet. *Ore Geol. Rev.* 70, 510–532.
- Zheng, Y.Y., Sun, X., Gao, S.S., Wu, S., Xu, J., Jiang, J.S., Chen, X., Zhao, Z.Y., Liu, Y., 2015c. Metallogenesis and the minerogenetic series in the Gangdese polymetallic copper belt. *J. Asian Earth Sci.* 103, 23–39.
- Zheng, Y., Zhang, L., Li, D.F., Kapsiotis, A., Chen, Y.J., 2015a. Genesis of the Dadonggou Pb–Zn deposit in Kelan basin, Altay, NW China: constraints from zircon U–Pb and biotite $^{40}\text{Ar}/^{39}\text{Ar}$ geochronological data. *Ore Geol. Rev.* 64, 128–139.
- Zhu, D.-C., Zhao, Z.-D., Niu, Y., Mo, X.-X., Chung, S.-L., Hou, Z.-Q., Wang, L.-Q., Wu, F.-Y., 2011. The Lhasa Terrane: Record of a microcontinent and its histories of drift and growth. *Earth Planet. Sc. Lett.* 301 (1–2), 241–255.